UNIVERSITÀ DEGLI STUDI DI PADOVA

Dipartimento di Tecnica e Gestione dei Sistemi Industriali

CORSO DI LAUREA IN INGEGNERIA DELL'INNOVAZIONE DEL PRODOTTO

TESI DI LAUREA TRIENNALE

Effects of Fe content on microstructural and mechanical wear properties in innovative aluminium alloys for piston applications in the automotive sector

Relatore: Ch.mo Prof. GIULIO TIMELLI

Correlatori: Ing. GIULIA SCAMPONE
Ing. YOZEN GYURSOY

Laureandi:
De Tomasi Leonardo, Loiacono Francesco, Marchetto Enrico,
Pasqualotto Francesco, Trevisan Pietro

UNIVERSITY OF PADOVA

Technique and Industrial Systems Management Department

PRODUCT INNOVATION ENGENEERING DEGREE COURSE

MCCXXII

THREE-YEAR DEGREE THESIS

Effects of Fe content on microstructural and mechanical wear properties in innovative aluminium alloys for piston applications in the automotive sector

Supervisor: Distinguished Prof. GIULIO TIMELLI

Assistant supervisors: Eng. GIULIA SCAMPONE
Eng. YOZEN GYURSOY

Undergraduates:
De Tomasi Leonardo, Loiacono Francesco, Marchetto Enrico,
Pasqualotto Francesco, Trevisan Pietro

Dedications

We would like to thank Giulia, Giacomo, Yozen and Professor Timelli for the technical support given during these last months.

Also, we want to thank our parents for giving us a chance to study and for helping us during the writing of the thesis.

Last but not least, we thank each other for assisting each other in this work.

Table of contents

ABSTRACT……………………………………………………………..…………11

FIGURES AND TABLES…………………………………………………….....13

INTRODUCTION…………………………………………………………...……17

Chapter 1

Al and its various forms

1.1 Alloys for pistons applications……………………………………...…..19
1.2 Fe-rich compounds………………………………………………...…23
    1.2.1 Morphology……………………………………………...….24
    1.2.2 Chemical composition…………………………………...….26
    1.2.3 Temperature…………………………………………........…27
    1.2.4 Mechanical and thermal properties……………...……....…..27
    1.2.5 Effects of alloying elements…………………………..….28

Chapter 2

Solidification analysis of an AlSi9Cu3(Fe) alloy

2.1 Alloy AlSi9Cu3(Fe)……………………………………..…………31
2.2 Analysis of alloys with the thermodynamic software………………..….33
    2.2.1 Alloy AlSi9Cu3(Fe 0,722 wt.%)……………………………….33
    2.2.2 Alloy AlSi9Cu3(Fe 1,223 wt.%)……………………………….38
    2.2.3 Considerations…………………………………………………43

Chapter 3

Sample preparation

3.1 Material preparation……………………………………………………..45
3.2 Casting…………………………………………………………………...46
3.3 Sample processing………………………………………………………49

Chapter 4

Tests and data analysis

4.1 Metallographic analysis…………………………………………………53
4.2 Acid etching and iron-analysis…………………………………………...54
    4.2.1 Considerations………………………………………………………58
4.3 Minitab analysis…………………………………………………………60
4.4 Hardness test……………………………………………………………..66
    4.4.1 Considerations………………………………………………………69
4.5 Wear test…………………………………………………………………71
4.6 Hardness and wear rate comparison……………………………………...74
4.7 Variance analysis………………………………………………………..76
4.8 Empiric equations………………………………………………………..79
    4.8.1 Procedure for the equations definition………………………………79
    4.8.2 Equation description…………………………………………………...81

CONCLUSIONS……………………………………………………………...85

BIBLIOGRAPHY……………………………………………………………….87

Abstract

The main goal of this study is to identify the effect of Fe content on microstructural and mechanical wear properties in aluminium alloys used in the automotive sector, specifically for pistons. The alloys analysed are EN AB-46000 (AlSi9Cu3(Fe)) with two different Fe wt.%: 0.722% e 1.223%; from now on, the alloys will be appointed to, respectively, as low-Fe and high-Fe alloy. Along with Fe wt.%, different casting temperatures are taken into account as well, in a range from 680°C up to 1030°C, with 70°C of difference between every temperature.

Wear test, hardness test and microstructural analysis are done on each sample, one for every temperature, to determine the mechanical and metallographic properties of both alloys. The influence on the test results of both iron amount and casting temperature is considered.

Moreover, the formation conditions for α-phase and β-phase (two Fe-rich compounds) are determined, again as function of casting temperature and Fe wt.%, with the target of obtaining an alloy with the least possible amount of β-phase, which is deleterious for the component performances.

The final objective is to determine two equations, one for hardness and one for wear rate, as functions of casting temperature and Fe wt.%.

The aim of chapter 1 is to gather literature concerning the subject of the thesis, then in chapter 2 the design of experiment is done, identifying the chemical compositions of the two alloys and defining the casting temperature and cooling rate.

Chapter 3 describes the process followed for the preparation of the samples that will undergo the experimental procedure, which is described in chapter 4, along with the data analysis, the retrieved considerations and empiric equations.

From the iron analysis the α-phase morphology varies as the bath temperature increases, in particular at higher temperatures it assumes a chinese-script form, while at lower ones it assumes a more polyhedral form. It is also found that β-phase decreases its quantity with the increase of the bath temperature.

As shown in the data, it seems that high Fe content is detrimental for hardness and wear resistance. If hardness and wear resistance are requested, the evidence of the data obtained suggests that the low-Fe alloy at a casting temperature of 820 °C results to be the best solution from an economical and performance perspective.

Figures and tables

Images:

Chapter 1:

Fig. 1.1: Tons of primary and secondary aluminium melted through the last decades compared to the worldwide demand
Fig. 1.2: emission comparison between cast iron and primary Al alloys with different % of secondary Al
Fig. 1.3: vehicle life cycle comparison between cast iron and primary Al alloys with different % of secondary Al
Fig. 1.4: Isometric view of a classic petrol engine's piston.
Fig. 1.5: wear rate effects on a piston
Fig. 1.6: The α-Fe particles which have polyhedral and star-like structures are shown in (a); in (b) are present polyhedral particles and Chinese script.
Fig. 1.7: The β-Fe phase has a lamellar morphology

Chapter 2:

Fig. 2.1: Low-Fe alloy whole composition

Fig. 2.2: Low-Fe alloy total solidification curve

Fig. 2.3: Low-Fe alloy aluminium solidification curve
Fig. 2.4: Al, Si, α-Fe, β-Fe eutectic
Fig. 2.5: Al, Si, Al7Cu4Ni eutectic
Fig. 2.6: Al, Si, Al2Cu, AlCu2Mg8Si6, Al7Cu2M, Al7Cu4Ni
Fig. 2.7: High-Fe alloy whole composition
Fig. 2.8: High-Fe alloy total solidification curve
Fig. 2.9: High-Fe alloy aluminium solidification curve
Fig. 2.10: Al, Si, α-Fe and β-Fe eutectic
Fig. 2.11: Al, Si, Al7Cu4Ni and Mg3Bi2 eutectic
Fig. 2.12: Al, Al2Cu, Al7Cu4Ni, Al7Cu2M and Al5Cu2Mg8Si6

Chapter 3:

Fig. 3.1: The cleaned die used for the casting process

Fig. 3.2: The furnace used to heat the material

Fig. 3.3: The preheat furnace used to dehumidify the die

Fig. 3.4: One of the samples obtained by the casting process

Fig. 3.5: Length at which the samples are marked (25 mm)

Fig. 3.6: Cutting machine used for material preparation

Fig. 3.7: Lapping machines used to polish and roughing the samples

Fig. 3.8: Embedding machine used to incorporate the alloy into the resin

Chapter 4:

Fig. 4.1: SDAS on the sample with low-Fe wt.% which is casted at 1030°C

Fig. 4.2: The high-Fe sample casted at 680°C after the chemical attack

Fig. 4.3: How the subsequently images are taken

Fig. 4.4: Microstructure of samples after the acid etching. (a) High Fe alloy at melting temperature of 750°C , (b) High Fe alloy at melting temperature of 820°C

Fig. 4.5: Microstructure of samples after the acid etching. (a) high-Fe alloy at melting temperature of 680°C, (b) low-Fe alloy at melting temperature of 680°C, (c) high-Fe alloy at melting temperature of 1030°C, (d) low-Fe alloy at melting temperature of 1030°C

Fig. 4.6: Fig. 4.6: Percentage amount of Fe-rich particles with a specific equivalent circle diameter for the low-Fe alloy

Fig. 4.7: Percentage amount of Fe-rich particles with a specific equivalent circle diameter for the High-Fe alloy

Fig. 4.8: The average equivalent circle diameter of the Fe-rich compounds as function of the casting temperatures

Fig. 4.9: The perimeter of the Fe particles of the two alloys as function of the casting temperatures

Fig. 4.10: Graphs of length and width of the Fe particles as function of the casting temperatures

Fig. 4.11: The roundness of Fe particles as function of the casting temperatures

Fig. 4.12: The aspect ratio of the Fe-rich compounds as function of the casting temperatures

Fig. 4.13: The durometer used for the hardness test

Fig. 4.14: The print formed on the sample after the hardness test seen through the lens

Fig. 4.15: Hardness comparison as function of the casting temperatures

Fig. 4.16: The tribometer used for the wear test

Fig. 4.17: The comparator used to verify the planarity of the samples before the wear test

Fig. 4.18: Wear rate comparison for the alloys, as function of the casting temperatures

Fig. 4.19: Wear rate of a hypereutectic alloy A390.

Fig. 4.20: Hardness and wear rate comparison, as function of the casting temperatures

Fig. 4.21: Porosities formed in the High-Fe alloy
Fig. 4.22: Balanced Analysis of Variance window
Fig. 4.23: Output of the Balanced Analysis of Variance
Fig. 4.24: Output of the Balanced Analysis of Variance for Hardness
Fig. 4.25: Compilation of factors in Create Factorial design
Fig. 4.26: Pareto Chart for Hardness
Fig. 4.27: Comparison between minitab results and experimental results as function of the casting temperatures
Fig. 4.28: Pareto chart for wear rate

Tables:

Chapter 1:

Tab. 1.1: alloy elements' price in USD per kg

Chapter 2:

Tab. 2.1: Alloys compositions obtained with iSparkTM optical emission spectrometer
Tab. 2.2: Alloy EN AB 46000 chemical composition; standard EN 1676:2020
Tab. 2.3: Low-Fe alloy composites start solidification temperatures

Tab. 2.4: Low-Fe alloy eutectics compositions

Tab. 2.5: Low-Fe alloy fourth eutectic
Tab. 2.6: Low-Fe alloy composites end of transformation temperature and final fraction
Tab. 2.7: High-Fe alloy composites start solidification temperatures
Tab. 2.8: High-Fe alloy eutectics compositions
Tab. 2.9: High-Fe alloy composites end of transformation temperature and final fraction

Chapter 3:

Tab. 3.1: Low-Fe Alloy and High-Fe alloy iron contents in wt.%

Tab. 3.2: Temperatures at which the various samples are casted

Tab. 3.3: Time requested for the furnace to reach the subsequent temperature and furnace heating rate

Tab. 3.4: Weight of each sample after the solidification process

Chapter 4:

Tab. 4.1: SDAS measurement for the different samples casted at different temperatures

Tab. 4.2: Comparison between the two alloys analyzed with different casting temperatures

Tab. 4.3: Micrographs taken from the acid etching at three different temperature(890°C, 960°C, 1030°C)

Tab. 4.4: The values obtained from the hardness test [HB] with the standard deviation for both the alloys at different casting temperatures

Tab. 4.5: Data used for the hardness minitab analysis

Tab. 4.6: the matrix obtained from Create Factorial Design

Tab. 4.7: the matrix with the Hardness values

Introduction

Aluminium has become a material economically competitive in engineering applications at the end of the 19th century.

There are 2 methods to produce it: the first one consists in the extraction of bauxite, which contains Al_2O_3, and subsequently the Bayer and the electrolytic processes (primary Al); in the other process aluminium is obtained by recasting primary aluminium's scrap (secondary Al).

In automobile industries high strength components are required, which must possess high temperature and elevated wear stress, but, at same time, they should satisfy weight requirements; therefore, it was decided to use alloyed aluminium.

In recent years, secondary Al alloys have seen an increasing demand, specifically for the automotive industry, since the production process is more eco-sustainable and economically affordable than the primary ones; in fact, the secondary Al process creates about 5 % of the CO_2 produced by the primary Al route, and saves about 90% of the energy produced by the primary processes.

Their excellent castability and high mechanical properties referred to the lightness are another reason why Al-based alloys use is increasing. Fe, Mn and Cr are elements commonly found in secondary aluminium alloys due to the recycling process. Generally, manganese and chromium enhance the alloy's mechanical properties and high temperature strength respectively, while iron is considered an impurity.

Throughout the last years the tribological properties of Al-Si alloys have been improved, particularly for pistons and cylinder blocks which are components that must withstand high wear rates and temperatures.

The target of this study is to analyse wear resistance variation of a secondary Al-Si-Cu alloy for automotive application by varying the iron weight (0,72-1,2%) and using different casting temperatures (680-1030°C); the objective is to obtain the higher wear resistance alloy for non-structural components, particularly for pistons.

This research should help the automotive industry to improve motor's performances, avoiding problems linked to pistons wear resistance, such as material removal from the area of the ring or dry running rubbing.

Chapter 1

Al and its various forms

1.1 Introduction of Aluminium

Nowadays there are two types of aluminium alloys: primary and secondary ones. Primary Al alloys have the highest purity level (99.9%) and, depending on the specific requests, several elements can be added to Al to improve the alloy properties, obtaining high performance alloys but very expensive to produce due to the Bayer and electrolytic processes.

Secondary alloys are cheaper to produce but contain several impurities that affect the alloy performance. In the last years, manufacturers tend to prefer these particular alloys because, as stated above, they are more economically convenient and have less impact on the CO_2 level in the atmosphere. Despite this, as of today there is not enough aluminium scrap to melt to sustain the demand, in fact only 28 million tons of secondary aluminium is produced yearly contrary to 70 million tons of primary aluminium.

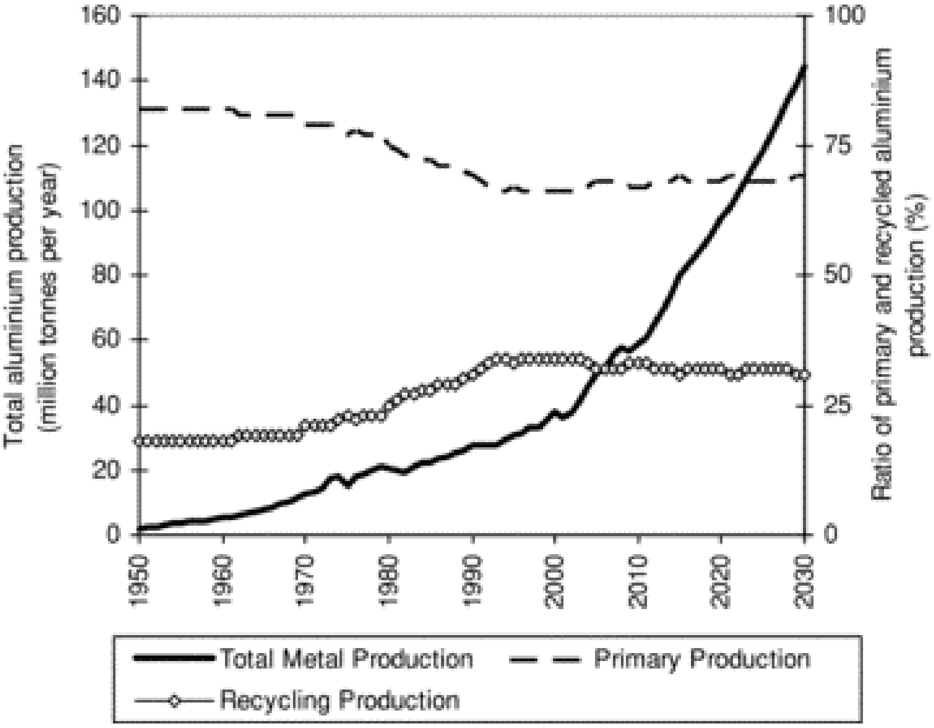

Fig. 1.1: Tons of primary and secondary aluminium melted through the last decades compared to the worldwide demand [1]

In terms of costs and emissions, cast-iron is more convenient than the primary Al alloys.

However, utilizing Al alloys made of primary and secondary aluminium, it is possible to match the cast iron emission during the production process.

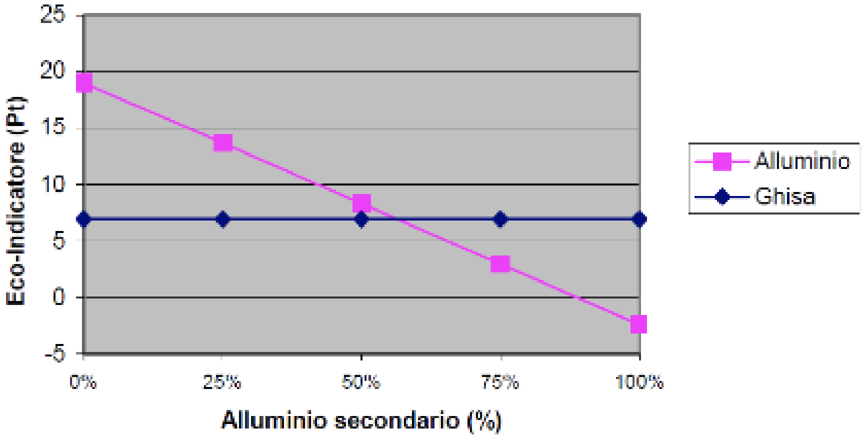

Fig. 1.2: Emission comparison between cast iron and primary Al alloys with different % of secondary Al [2]

Moreover, using aluminium, that is much lighter than cast-iron, in engines for the automotive industry, CO_2 emissions decrease even more because less fuel is consumed to run the same distance.

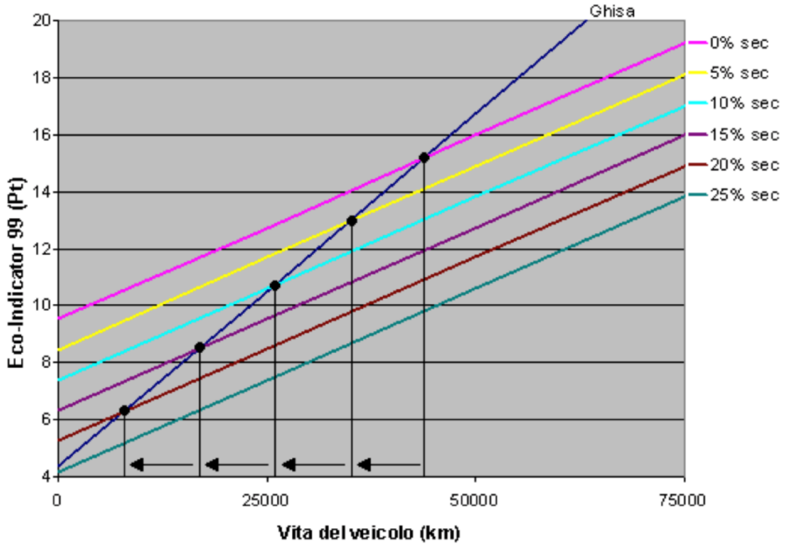

Fig. 1.3: Vehicle life cycle comparison between cast iron and primary Al alloys with different % of secondary Al [3]

The major problem in secondary die cast Al alloys is linked to impurities and iron is one of the most present, among others.

The stress incurred by a thermal engine's piston are compression, wear stress, shear strain and thermal solicitation.

In particular, temperatures reached in the combustion chamber can exceed 1000 °C; such temperatures are unsustainable for a piston's crown, because aluminium generally melts at 660 °C. For this reason, pistons made with Al-Si die cast alloys are anodized in order to form a plate of 30-50 microns of alumina in that area.

Moreover, heat exchange is promoted in the pistons' skirt by making pistons with thin thickness, accompanied by a circuit of cooling water.

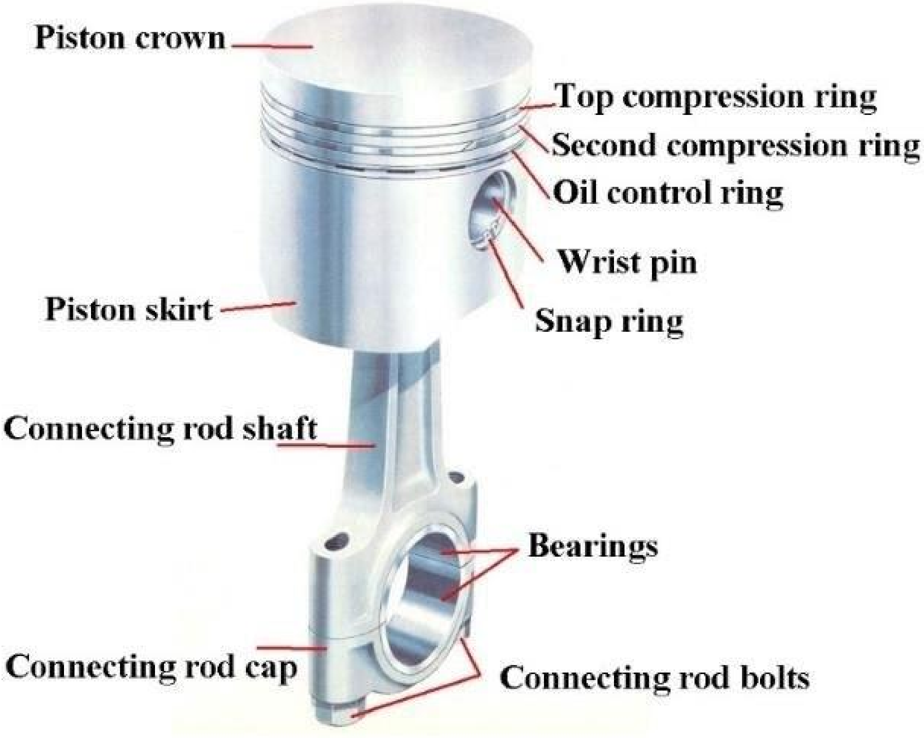

Fig. 1.4: Isometric view of a classic petrol engine's piston [4]

In addition to the thermal stress, another important factor is wear resistance, which is the most critical one.

Wear rate is the progressive removal of material from one or both surfaces in contact and in relative motion with each other.

Therefore, wear resistance is fundamental for non-structural components, particularly for pistons, since their job is to continuously slide inside the cast iron cylinder block, which hardness is higher than that of pistons.
To counter this issue, seals or lubricants can be used. Nevertheless, the lubricant oil might enter the combustion chamber and worsen the combustion process, leading to lower performances. Therefore, oil lubricants use is reduced to its minimum.
The best solution to counteract the combustion issue would be dry running, which is not completely doable, therefore it is necessary to enhance the piston's hardness enough to match the cylinder block one in order to reduce the piston's wear rate.

Fig. 1.5: *Wear rate effects on a piston [5]*

To improve the aluminium alloy hardness, thermal treatments can be done, but these processes only increase the hardness by a small amount, which is not sufficient. Another method is the addition of specific elements to the alloys, such as Si, Ni, V, Zr, Ti, by which hardness and thermal resistance of the alloy prove to be increased. The downside of these elements is their high costs that limit their usage. Due to this issue, it is customary to take advantage of the elements that are already present inside the secondary alloy, such as Fe and Mn, which both increase some material properties (in a low percentage) and are less expensive too. [Tab.1.1]

Tab. 1.1: *Alloy elements' price in USD per kg [6]*

	Si	Ni	V	Zr	Ti	Fe	Mn
Price [USD/kg]	1.70	13.9	357÷ 385	35.7÷ 37.1	11.1÷ 11.7	0.424	1.82
Date	2019	2019	2020	2020	2020	2020	2019
Source	Preismonitor	Preismonitor	SMM	SMM	SMM	SMM	Preismonitor

1.2 Fe-rich compounds

Fe-rich compounds present an issue related to its different morphologies which could weaken the material. One of these is the β-phase which shows an acicular form that is harmful because it causes a focused stress on the needles' tips, which decreases the mechanical properties, in particular the ductility.

On the other hand, iron also produces another phase, defined as α-phase. This compound presents a morphology that has a better stress distribution, therefore it is less deleterious than β-phase.

The problem is that α-phase is metastable, while the β one is thermodynamically stable, therefore its formation is promoted.

Thus far, there are various methods to promote α-phase:

- modifying the chemical composition, adding to the material elements that stabilize the α-phase; however, some elements could be really expensive thus making a secondary alloy no longer advantageous to use;

- adding Sr which inhibits the AlP sites, where β-phase nucleates;

- increasing the cooling rate. By cooling the component through a path of non-equilibrium stages, the formation of the metastable phase is promoted. To operate in this way, the most important parameter is the component's thickness. In fact, the thinner the component, the higher the cooling rate will be. However, the component's rigidity is influenced by its thickness: if it's too thin, the rigidity will be too low for the component to be used in applications like those of pistons;

- acting on the superheat temperature. Increasing the gap between the liquidus line of the alloy and the melt temperature at which the alloy is casted enhances the formation of α-phase.

The tendency of AlSi9Cu3 alloys to form primary Fe-rich particles can be predicted by the sludge factor (SF) equation. Every Fe-rich compound that solidifies before the α-Al dendrites is defined as sludge. The empirical sludge factor equation is defined as:

$$Sludge\ Factor\ (SF) = (1 \times wt.\%Fe) + (2 \times wt.\%Mn) + (3 \times wt.\%Cr)[7]$$

When Fe, Mn, or Cr wt.% is increased, a coarser sludge form. [7]
Primary Fe-rich compounds are bigger compared to secondary ones, due to the presence of liquidus around the particles which allow sludge to grow. The larger dimensions, so the coarse grain, decrease mechanical properties of the alloy.

1.2.1 Morphology

In Al-Si-Cu alloys Fe rich compounds can assume different morphologies: needle-like, polyhedral structure, star-like and the convoluted arm structure ("Chinese-script"). The first one is associated to the β-phase while the others to the α-phase. Under equilibrium conditions the β-phase is thermodynamically stable while the α-phase is metastable. [8]
The β-phase platelets have a monoclinic lattice and lamellar morphology whereas the polyhedral and star-like structure show up when α-phase forms as a primary phase with an hexagonal lattice, before the aluminium dendrites begin to solidify. [8] The Chinese-script, which has a cubic structure, occurs after the aluminium dendrites have already begun to solidify. [9]

According to [10] an increase in the cooling rate can lead to the inhibition of β-Fe formation and to the promotion of α-Fe precipitation. Generally, the β-Fe phase is obtained through cooling rates lower than approximately 20 °C/s [8]; α-Fe particles show "Chinese-script" morphology at increasing cooling rates and, at lower cooling rates, they exhibit the polyhedral or star-like ones. [11]

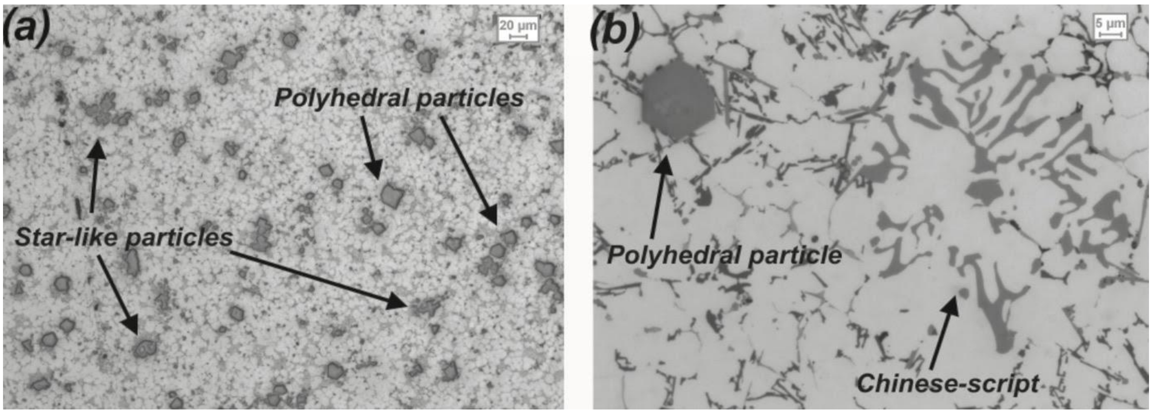

Fig. 1.6: *The α-Fe particles which have polyhedral and star-like structures are shown in (a); in (b) are presented polyhedral particle and Chinese script [12]*

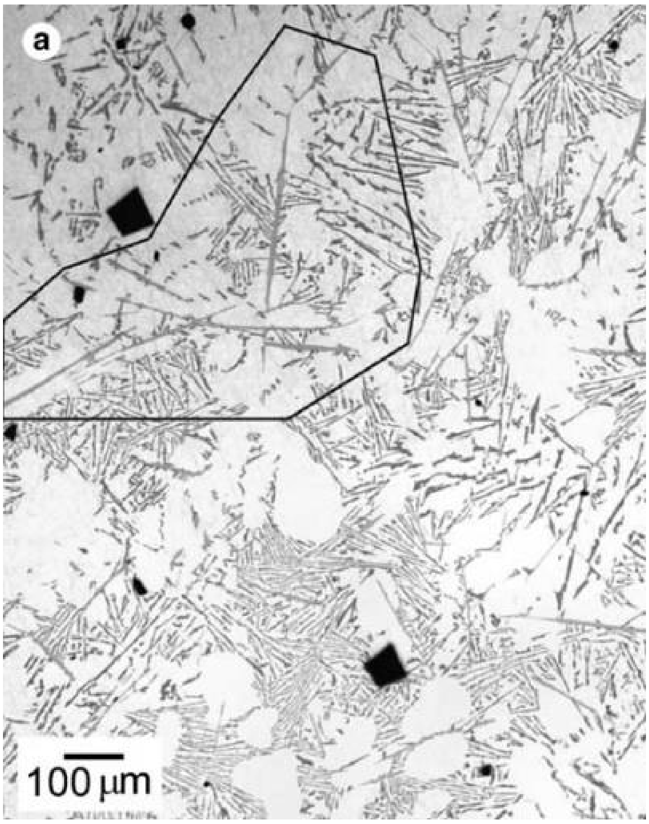

Fig. 1.7: *The β-Fe phase has a lamellar morphology [13]*

1.2.2 Chemical composition

The alloy's chemical composition affects sludge morphology.

The most β-Fe enriched alloys were revealed to be the alloys with the relative higher Fe content. Al_5FeSi generally is the β-phase stoichiometry composition, nonetheless Fe atoms can be replaced by Mn and Cr, in the maximum amount of 3.0 wt%. In this case the structure becomes β-Al_5(Fe, Mn, Cr)Si. With reference to α-phase, high precipitation of such phase occurs when Fe:Mn ratio is lower than 2. [7] Finally, higher Fe amounts generally lead to lower fluidity. [8]

The eutectic grain is influenced by the Fe content. In fact, β-phase and the Al-Si eutectic share a common nucleant particle, AlP. β-phase, that forms prior to the Al-Si eutectic, nucleates on AlP. Consequently, at the eutectic temperature there are less cores available for the eutectic, so the eutectic grain size increases. [11]

However, if the α-phase is promoted at the expense of the β-phase, more nucleation sites will be provided for the eutectic, therefore, the eutectic grain size will decrease. [11]

Indeed, at the beginning of the solidification process, higher levels of Fe lead to a temperature increase, due to the recalescence phenomenon which promotes an increase of the grains size. [8]

Another correlated factor with the Fe content is the porosity. In particular, the use of more Iron, leads to a larger size of the eutectic grain. Moreover, the β-phase may block the feed paths, for the friction caused by his dendritic arms. These two facts reduce the fluid's mobility and increase the porosity influencing its shape. Hence, growing Fe content in the alloy causes a deterioration of the liquid fluidity. [11][14]

Lastly, there is no relation between the Fe content and the morphological variation of the sludges, as well as between the Fe:Mn ratio and the sludge factor. [7]

1.2.3 Temperature

An empirical equation determines the temperature below which Fe-rich particles tend to form in AlSi9Cu3 alloys; this equation is defined as follows:

$$Temperature\ [°C] = 645.7 + 34.2(wt.\%Fe)^2[7]$$

Also, the melt temperature influences the process. Specifically, it affects the morphology of Fe-rich particles. This is due to the Al oxide that covers the bath surface, which acts as a nucleant for sludge. The structure of the Al oxide is influenced by the temperature.

Different melt temperatures change the type of oxide that forms. When the melt is superheated to temperatures higher than 850°C, the cubic metastable oxide γ-Al_2O_3, which is a nucleant for the β-phase, transforms into the hexagonal stable α- Al_2O_3, which promotes the formation of α-phase. [7] Also, the precipitation of finer particles is obtained thanks to higher melt temperature, along with higher cooling rate. [8]

The metal-matrix-composite surface resistance is influenced by temperature too. High temperature promotes higher resistance since it accelerates the oxidation of the residual metal, increasing wear resistance as well. [15]

1.2.4 Mechanical and thermal properties

Generally, an increase of Fe wt% is detrimental for fracture strain but enhances yield strength. [8]

With the increase of Fe wt% a reduction of the alloy fatigue resistance is observed and this phenomenon is more significant for grains with larger dimensions. [8]

The β-Al_5FeSi platelet size (average maximum length) is deleterious to alloy ductility and tensile strength. [14]

Hardness and wear resistance improve when Fe is added. Addition of iron up to 1.2 wt.%, along with Mn, leads to formation of plate-like phase (α-Fe), and wear resistance of the alloy improves significantly. [16]

The different sludge morphology seems to not be reflected in the hardness value. [15]

Regarding thermal properties, the presence of α-phase enhances the alloy properties at elevated temperature, such as thermal stability, hot strength, lower thermal expansion and lower specific heat capacity. [16]

1.2.5 Effects of alloying elements

The impact of Fe on the alloy is discussed throughout all the work, so, following, are listed the effects of the main alloy elements, which are kept unchanged between the two alloys. Every element added induces a modification to the alloy's characteristics.

The influence of the main elements is briefly described below:

- **Si**: its presence increases castability and, contemporarily, decreases the shrinkage and brittleness at high temperature; moreover, Si deteriorates the alloy's machinability due to the formation of small grains of Mg2Si in cooperation with Al2Cu, which are harmful for the tool's cutting edge.

- **Cu**: an increasing content of Cu leads to an improvement of mechanical strength and hardness of the alloy. However, ductility is penalized and for this reason a maximum of 12 wt.% of Cu is dissolved in the alloy. The existence of a blocky Al2Cu phase affects the overall mechanical properties of the alloy. Copper atoms are occupied by blocky Al2Cu and cannot be dissolved into the Al matrix, weakening the ageing strengthening response. Moreover, the blocky structure can be the crack source during loading, decreasing the ductility. Furthermore, the main limitation of Cu is the decay of the corrosion resistance in the alloy, even if it is present in low quantity. About the technological features, the alloy's castability varies along with the Cu concentration; specifically, the maximum value of castability occurs in correspondence of the eutectic.

- **Mn**: entails the formation of larger grains in the alloy during the thermal treatment T6 (solubilization, homogenization and recrystallization). Nevertheless, Mn is used to enhance the alloy mechanical properties.

Moreover, it is used to form intermetallic compounds which embrittle the alloy but reduces the negative effect of Fe on the corrosion resistance of the alloy.

- **Mg**: increasing Mg wt.% causes an enhancement of the alloy's corrosion resistance. Significant improvements of the mechanical properties, such as ductility or machinability, are detected in the alloy if the amount of Mg is higher than 8 wt.% and the alloy is subjected to hardening and tempering thermal treatment. However, it has high reactivity with oxygen; therefore, when they react, MgO_2 forms, leading to a reduction of Mg wt.% in the alloy composition.

The minor elements are:

- **Ni:** it increases the resistance to high temperature.
- **Pb, Sn, Bi:** are used to facilitate mechanical processes. Sn is also used in high content where anti-friction characteristics are requested.

The main modifying element is:

- **Ti:** is used to promote the grain refining.

The elements considered as impurities are:

- **Zn**: increases castability and machine tool machinability but it also increases the fragility at high temperature and the withdrawal coefficient. This element combined with magnesium could form high resistance alloys.
- **Cr**: despite it could confer high temperature resistance, it is usually considered as an impurity due to its contribution to the formation of phases which are deleterious to the alloy's ductility and tensile strength.

Chapter 2

Solidification analysis of an AlSi9Cu3(Fe) alloy

2.1 Alloy AlSi9Cu3(Fe)

The examined alloys are analyzed with the mass spectrometer Thermo ScientificTM ARL 3460 iSparkTM optical emission spectrometer (OES), with a wavelength ranging from 130 nm to 780 nm.

Tab. 2.1: *Alloys compositions obtained with iSparkTM optical emission spectrometer*

	Al wt.%	Si wt.%	Fe wt.%	Cu wt.%	Mn wt.%	Mg wt.%	Zn wt.%	Cr wt.%	Ni wt.%	Ti wt.%	Pb wt.%	Sn wt.%	V wt.%	Bi wt.%	Zr wt.%	Sr wt.%	Na wt.%
Low Fe Alloy	86,66	8,4	0,72	2,33	0,217	0,193	1,051	0,056	0,053	0,037	0,092	0,033	/	0,034	0,008	< 0,0001	< 0,0001
High Fe Alloy	86,57	8,11	1,22	2,35	0,214	0,188	1,03	0,055	0,051	0,037	0,089	0,03	/	0,033	0,007	< 0,0001	< 0,0001

The amount of P of both alloy, which is not specified in the chart above, is 0.0015 wt.%.

According to the standard UNI EN 1676 and 1706, the two alloys are included in the following table,which represent and define the alloy EN-46000 composition:

Tab2.2: *Alloy EN AB 46000 chemical composition; standard EN 1676:2020*

Alloy designation			Si wt.%	Fe wt.%	Cu wt.%	Mn wt.%	Mg wt.%	Zn wt.%	Cr wt.%	Ni wt.%	Ti wt.%	Pb wt.%	Sn wt.%	Others	
Numerical	Chemical symbols													Each	Total
EN-AB46000	EN-AB-AlSi9Cu3(Fe)	MIN.	8.0	0.6	2.0	-	0.15	-	-	-	-	0	-	0.05	0.25
		MAX.	11.0	1.1	4.0	0.55	0.55	1.2	0.15	0.55	0.20	0.29	0.15		

Generally, the most common light alloys used in the automotive and aerospace sectors are the hypereutectic Al-Si alloys due to their good corrosion and wear resistance, low density, low thermal expansion and significant colability. [17]

However, in conventional melting processes it is difficult to control the dimension of the Si grain that result coarse and, consequently, detrimental for the mechanical properties.

Fine grains can be obtained by specific treatment which usually are expensive or not useful in specific cases.

For those reasons, hypoeutectic Al-Si alloys has been chosen for this case study. This class of alloys is made with silicon (5% - 13%) and copper (2% - 5%), the aim of the last one is to increase mechanical properties through a thermal treatment of hardening and ageing. Usually, Mg is added up to a maximum concentration of 1.5% to enhance the velocity of ageing, without this element the velocity of this thermal process would be too slow and uneconomical.

Alloys with high Si wt.% show an elevated wear resistance, for this property they are largely used for production of engine blocks and for pistons in the automotive sector. [18]

2.2 Software analysis

These alloy’s thermodynamic analysis was carried out through JmatPro software. The solidification calculation was initialized from a starting temperature of 1030 °C with a 0.5 step value between each temperature; hence, the tolerance on the temperature values will as well be ± 0.5.

From now on the AlSi9Cu3 (Fe 0,722 wt.%) will be referred to as low-Fe alloy and the AlSi9Cu3 (Fe 1.223 wt.%) as high-Fe alloy. Furthermore, referring to Al_7Cu_2M compound, the “M” stands for “metal”, specifically iron.

2.2.1 AlSi9Cu3(Fe 0,8 wt.%) alloy

In low-Fe alloy different compounds are formed during solidification. The whole composition is shown in Fig. 2.1:

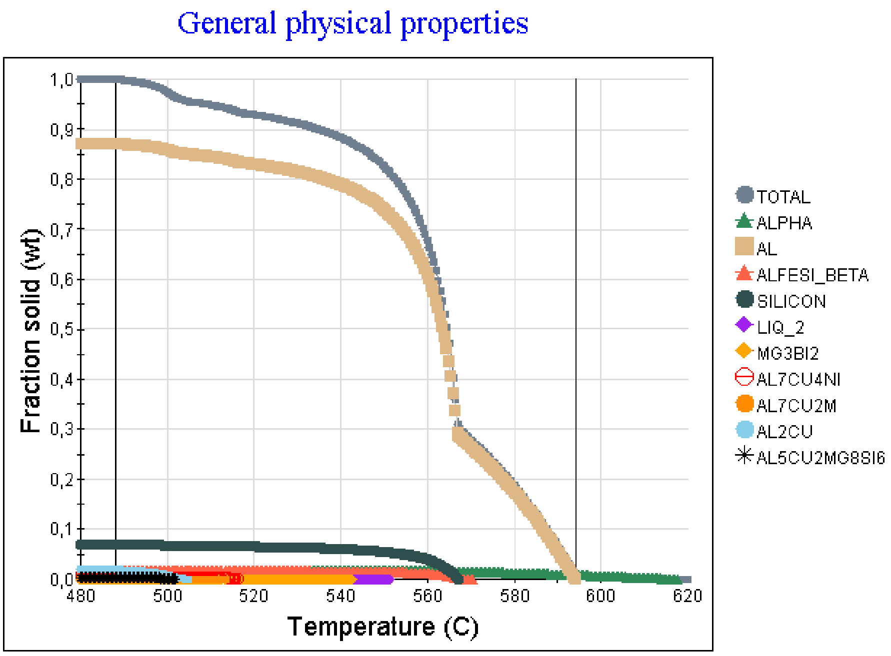

Fig. 2.1: Low-Fe alloy complete composition

First of all, the solidification process starts at 617°C with the formation of α-phase followed by Al at 594°C. Subsequently, the β-phase and Si are formed respectively at

570°C and 567°C; Al_2Cu is formed instead at 504°C. The remaining compounds that form are reported in Tab.2.3.

Tab. 2.3: *Low-Fe alloy composites start solidification temperatures.*

Compounds	Solidification start [°C]
α-Fe	617,15
Al	594,12
β-Fe	570,4
Si	567,5
Al_7Cu_4Ni	516,55
Al_7Cu_2M	513,4
Al_2Cu	504,71
$Al_5Cu_2Mg_8Si_6$	501,65

The total solidification curve indicates conditions formation of all the compounds in each alloy. Besides the three areas show the solidification's phenomenon occurs at an almost constant temperature.

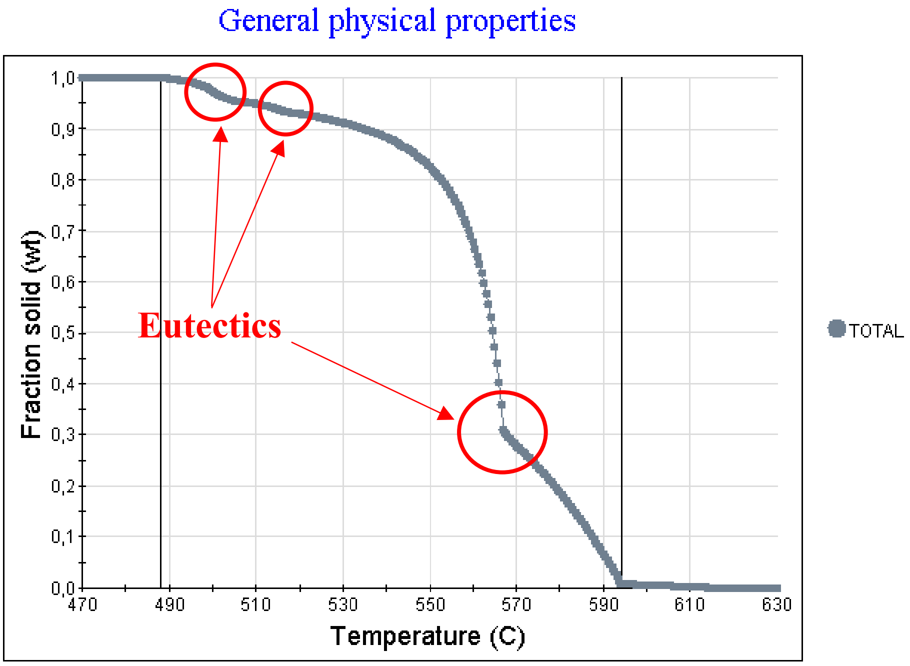

Fig. 2.2: *Low-Fe alloy total solidification curve*

The formation of three eutectics is indicated by the presence of compounds with a lower melting temperature than that of the components that constitute them. The eutectics that form in these alloys are mainly composed of Al and Si. [Tab. 2.4]

Tab. 2.4: *Low-Fe alloy eutectics compositions*

Compounds	Eutectic at 567°C	Eutectic at 516°C	Eutectic at 501°C
Al [wt.%]	94,42	92,66	91,83
α-Fe [wt.%]	4,82		
β-Fe[wt.%]	0,58		
Si [wt.%]	0,18	7,34	7,22
Al2Cu [wt.%]			0,49
Al5Cu2Mg8Si6 [wt.%]			0
Al7Cu2M [wt.%]			0,04
Al7Cu4Ni [wt.%]		0	0,43

For better comprehension aim, Al will be omitted from the eutectic graphs. Therefore, a graph exclusively for the eutectics in the Al curve is presented [Fig.2.3]

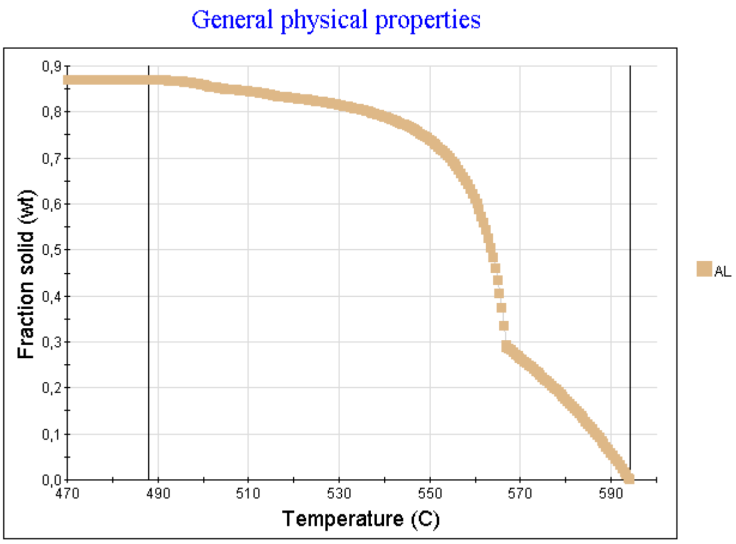

Fig. 2.3: *Low-Fe alloy aluminium solidification curve*

The first eutectic is formed between Al, Si, α-Fe, β-Fe at 567°C. [Fig.2.4]

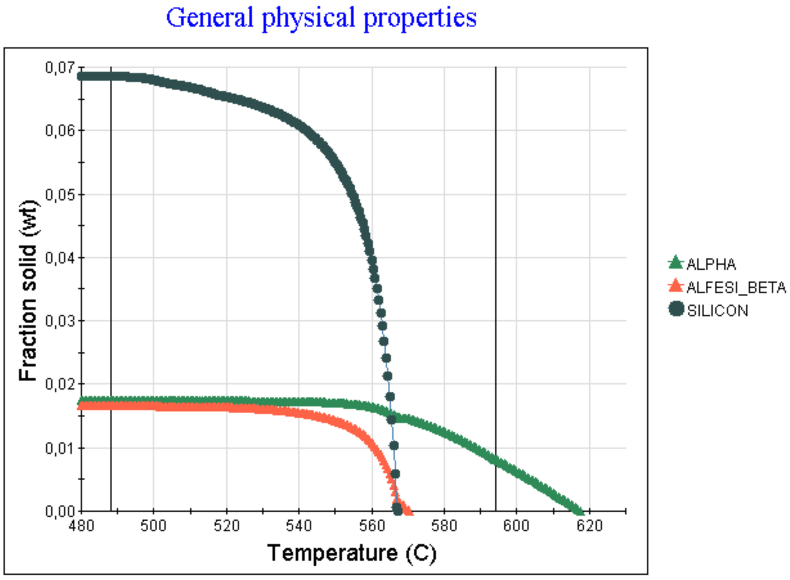

Fig. 2.4: Al, Si, α-Fe, β-Fe eutectic

The second eutectic is formed among Al, Si, Al_7Cu_4Ni at the temperature of 516,5°C. [Fig.2.5]

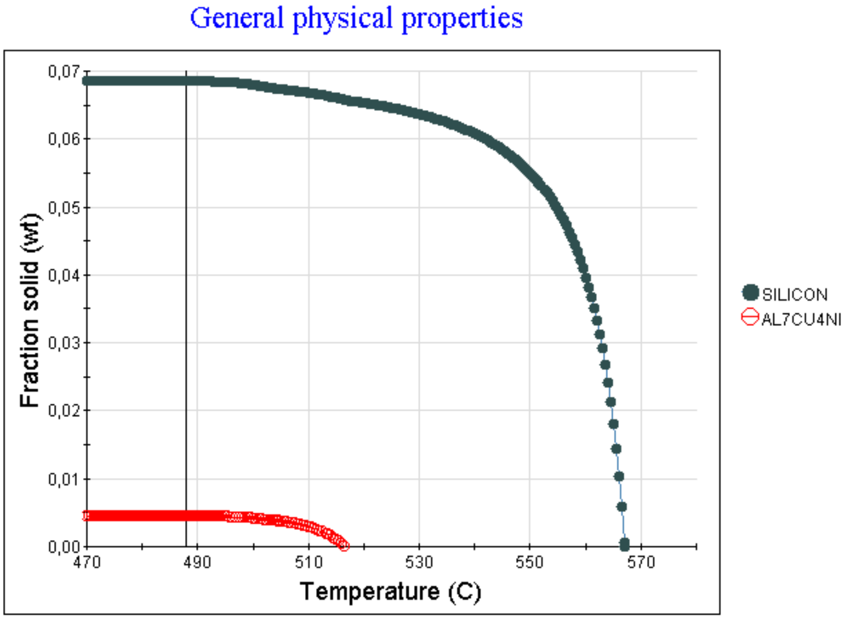

Fig. 2.5: Al, Si, Al_7Cu_4Ni eutectic

The third eutectic is formed between Al, Si, Al_2Cu, $AlCu_2Mg_8Si_6$, Al_7Cu_2M, Al_7Cu_4Ni at 501,5°C. [Fig.2.6]

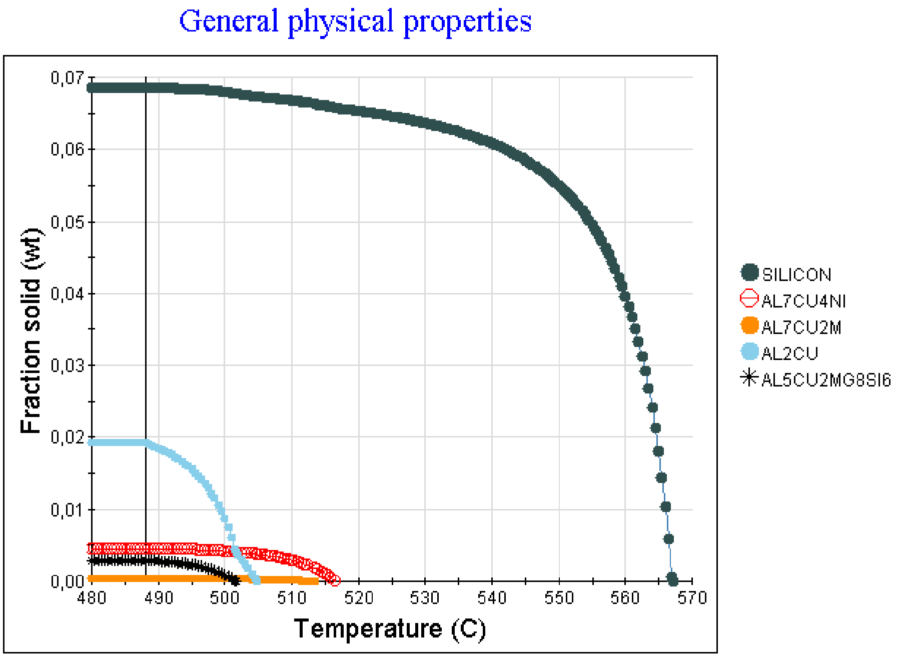

Fig. 2.6: Al, Si, Al_2Cu, $AlCu_2Mg_8Si_6$, Al_7Cu_2M, Al_7Cu_4Ni eutectic

The fourth eutectic forms and is composed by Si and Mg_3Bi_2, but presents a very little content of Mg_3Bi_2, as shown in Tab.2.5. However, the Mg_3Bi_2 amounts are negligible for the alloy studied.

Tab. 2.5: Low-Fe alloy fourth eutectic

Compounds	Final fraction in the eutectic at 505°C[wt.%]	Final fraction [wt.%]
Si	6,673	6,86
Mg_3Bi_2	2,3E-4	2,43E-4

The final fractions and final formation temperature of all the compounds analysed in low Fe alloy are reported in the following table [Tab. 2.6].

Tab. 2.6: Low-Fe alloy composites end of transformation temperature and final fraction

Compounds	End of the transformation [°C]	Final fraction [wt.%]
α-Fe	518	1,74
β-Fe	496	1,66
Al	491	87
Mg_3Bi_2	491	2,43E-02
Silicio	489	6,86
Al_7Cu_4Ni	488	0,48
Al_7Cu_2M	488	4,54E-02
Al_2Cu	488	1,93
$Al_5Cu_2Mg_8Si_6$	488	0,292

2.2.2 AlSi9Cu3(Fe 1,2 wt.%) alloy

The analysis obtained by JMatPro shows, in Fig.2.7, the whole solidification curves of the high Fe alloy compounds.

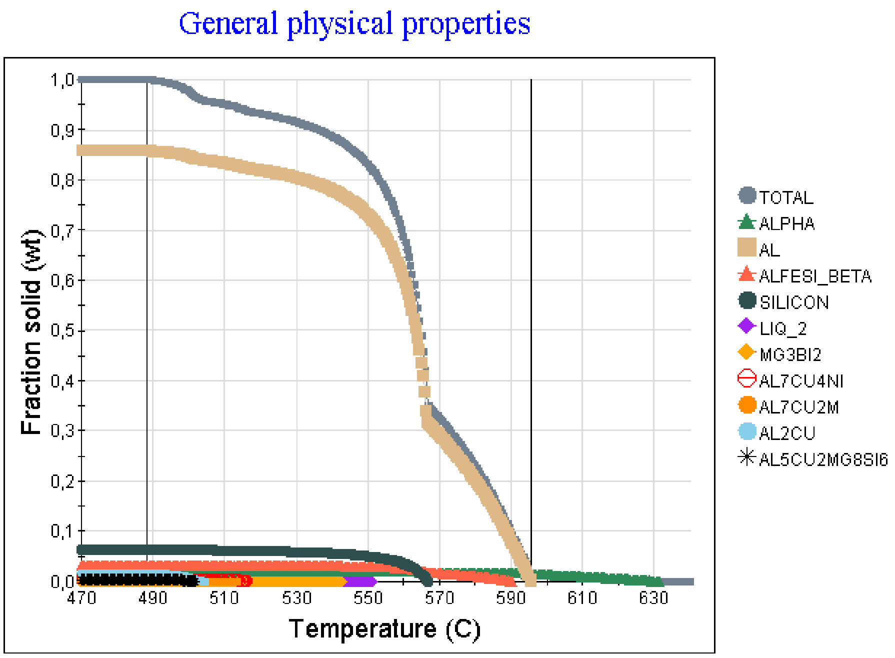

Fig. 2.7: High-Fe alloy whole composition

In this alloy, which contains 1,223wt% of Fe, as shown in Tab.2.7, α-Fe and β-Fe phases start their solidification at higher temperature than low-Fe alloy; the other compounds' solidification temperature are almost unchanged.

Tab. 2.7: High-Fe alloy composites start solidification temperatures

Compounds	Solidification start[°C]
α-Fe	631,3
Al	595,74
β-Fe	590,56
Si	567
Mg_3Bi_2	542,81
Al_7Cu_4Ni	516
Al_7Cu_2M	513,17
Al_2Cu	504,4
$Al_5Cu_2Mg_8Si_6$	501

The total curve [Fig2.8] suggests the presence of 4 eutectic points: 567°C, 516°C, 505°C and 501°C. This alloy presents one more eutectic point at 505°C, which is presented at the same temperature of the fourth eutectic of low-Fe alloy; in high-Fe alloy, the wt.% of compounds at this eutectic is more relevant for the study.

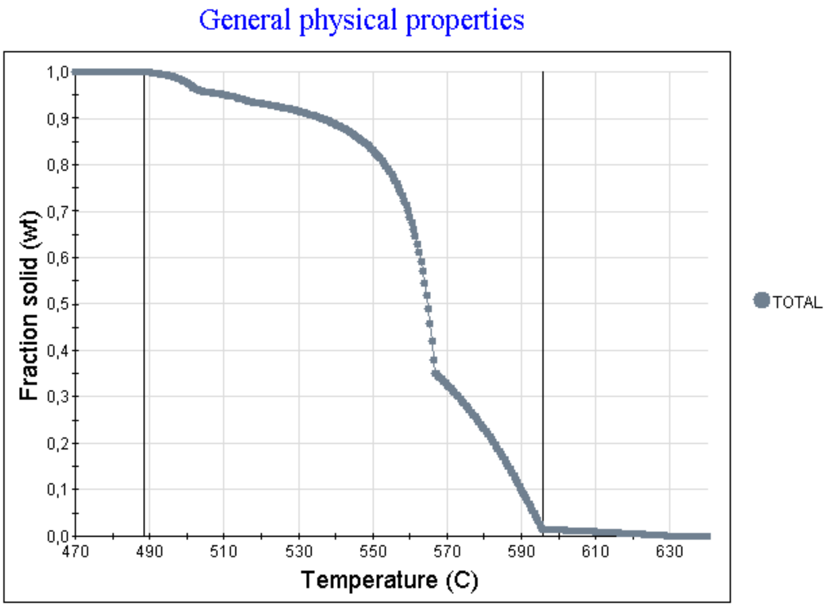

Fig. 2.8: High-Fe alloy total solidification curve

Particularly, the following compounds form these eutectics [Tab. 2.8]:

***Tab. 2.8:** High-Fe alloy eutectics compositions*

Compounds	Eutectic at 567°C	Eutectic at 516°C	Eutectic at 504°C	Eutectic at 501°C
Al[wt.%]	89,91	93,07		92,58
α-Fe[wt.%]	5,11			
β-Fe[wt.%]	4,97			
Si[wt.%]	0	6,91	94,27	6,92
Al2Cu [wt.%]				0,04
Al5Cu2Mg8Si6 [wt.%]				0
Al7Cu2M [wt.%]				0,03
Al7Cu4Ni [wt.%]		0	5,37	0,42
Mg3Bi2 [wt.%]		0,02	0,34	

For a better comprehension, Al will be omitted from the eutectic graphs, therefore a graph exclusively for the eutectics in the Al curve is presented. [Fig.2.9]

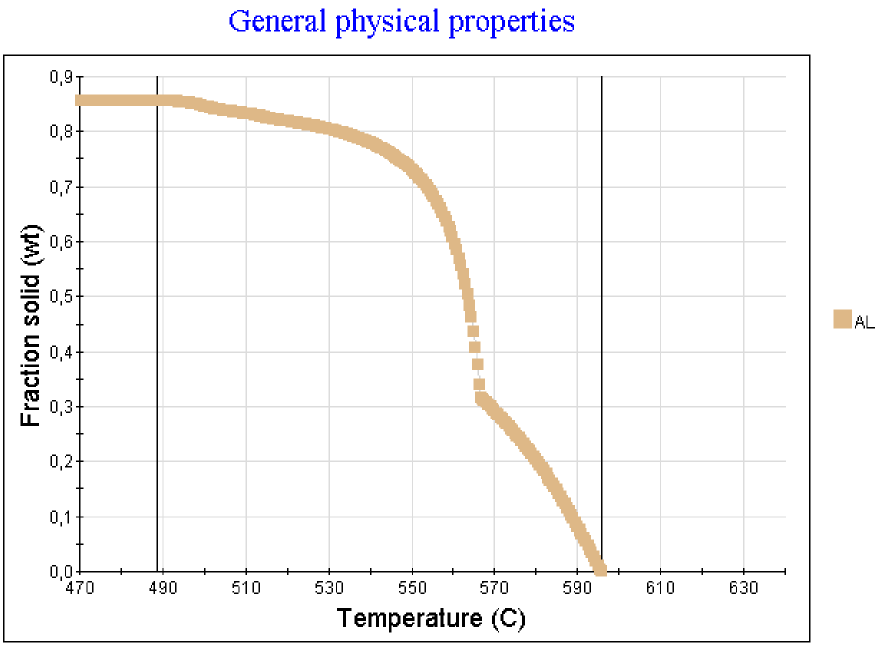

***Fig. 2.9:** High-Fe alloy aluminium solidification curve*

In Fig. 2.10 is represented the eutectic at 567°C among Al, Si, α-Fe and β-Fe.

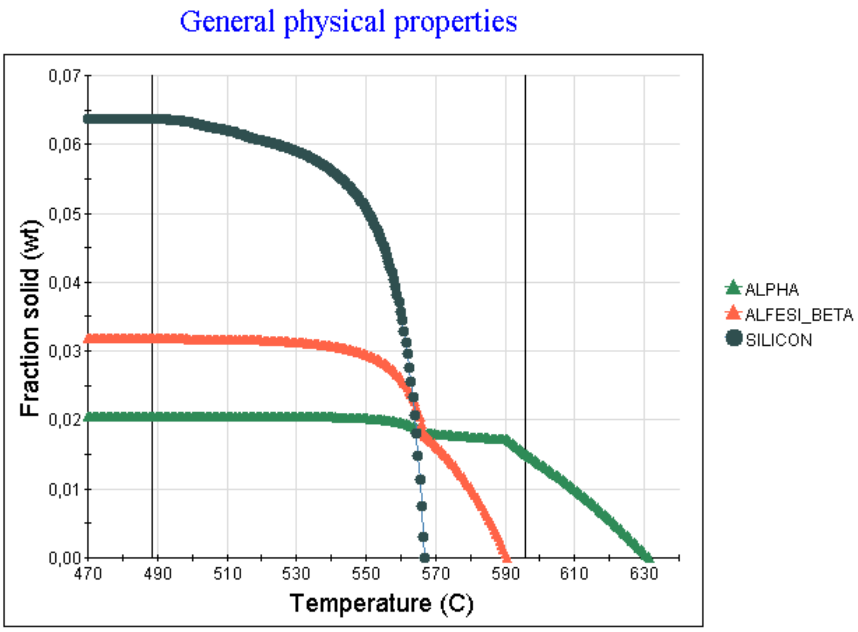

Fig. 2.10: *Al, Si, α-Fe and β-Fe eutectic*

The second eutectic detected is formed by Al, Si, Al_7Cu_4Ni and Mg_3Bi_2 at a temperature of 516 °C

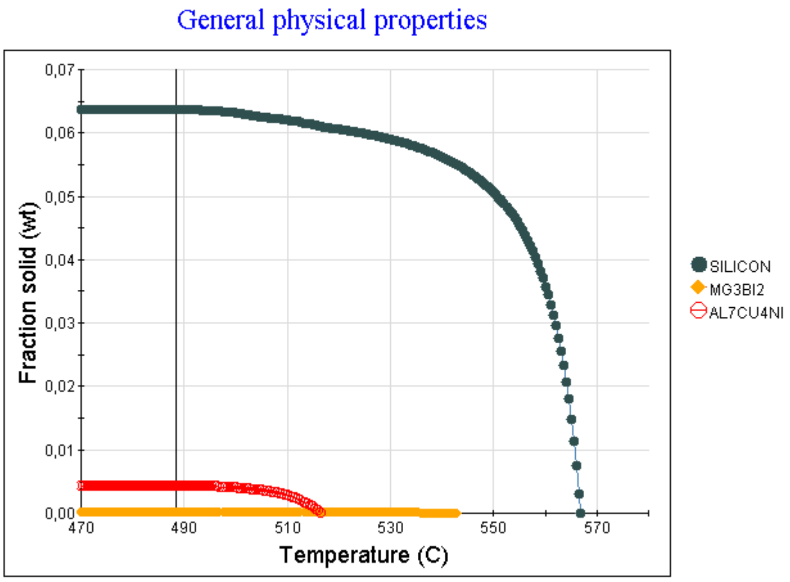

Fig. 2.11: *Al, Si, Al_7Cu_4Ni and Mg_3Bi_2 eutectic*

The eutectic at 504°C between Si, Al7Cu4Ni and Mg3Bi2 is the third and, since the Al is not considered in the eutectics' graphs for visual/comprehension reasons, the chart of this eutectic appears to be the same as in Fig. 2.11.

The fourth and last eutectic of the high-Fe alloy is formed by Al, Al_2Cu, Al_7Cu_4Ni, Al_7Cu_2M and $Al_5Cu_2Mg_8Si_6$.

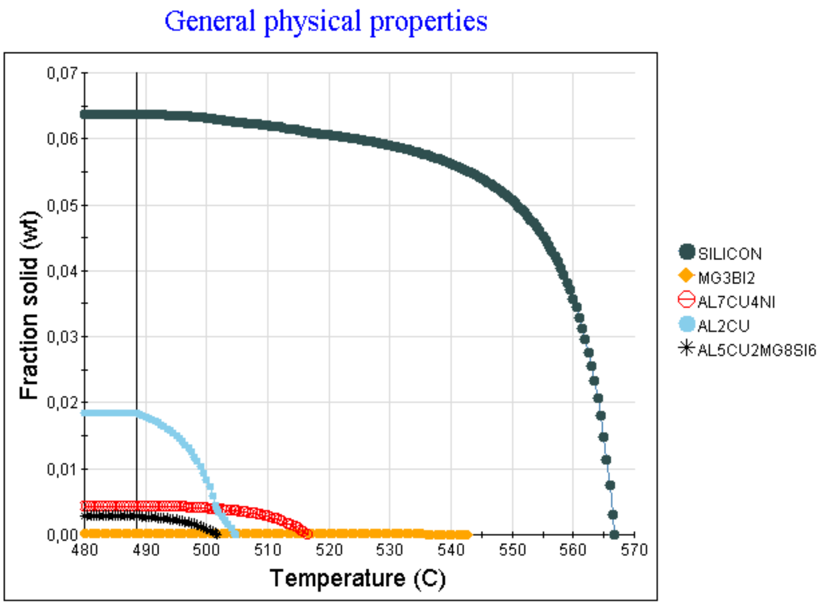

Fig. 2.12: *Al, Al_2Cu, Al_7Cu_4Ni, Al_7Cu_2M and $Al_5Cu_2Mg_8Si_6$ eutectic.*

Ultimately, the final fractions and final formation temperature of all the compounds of high-Fe alloy are examined and noted in the next table. [Tab.2.8]

Tab. 2.8: *High-Fe alloy composites end of transformation temperature and final fraction.*

Compounds	End of the transformation [°C]	Final fraction[wt.%]
Al	493	86
α-Fe	498	2,06
β-Fe	499	3,18
Si	490,5	6,63
Al_2Cu	488,5	1,84
$Al_5Cu_2Mg_8Si_6$	488,5	0,291
Al_7Cu_4Ni	488,5	0,43
Al_7Cu_2M	488,5	0,04
Mg_3Bi_2	488,5	0,0235

2.2.3 Considerations

In both alloys the compound that solidifies first is α-phase. It is important to control this phenomenon because it is necessary to avoid the compound's formation inside the furnace; if the α-phase forms it will decant on the crucible floor and damage it, decreasing its thermal conductivity and deteriorating the alloy's performance as well.

As expected, as the iron content increases, the quantity (wt.%) of Fe-rich compounds increases as well. In particular, the wt.% of α grows from 1,74 wt.% in low Fe alloy to 2.06 wt.% in the second one and β grows from 1,66 wt.% to 3.18 wt.%. Thus, in accordance to paragraph 1.2.2, the increase of β-phase is more significant than that of α-phase; specifically, α increased by only 18.4 %, while β shows an increment of 91.6%.

In the high Fe alloy, the pure Al final fraction decreases its wt.% because it is used for the α and β formation, which requests a higher wt.% of Al due to the increased presence of iron.

Moreover, the formation temperatures of Fe-rich compounds (both α and β) rise with the increase of Fe wt. % in the alloy; therefore, higher formation temperatures are shown in the high-Fe alloy.

In the high-Fe alloy the transformation temperature range of both α and β results to be enhanced; the α one increases from 99°C to 133°C, while for β it increases from 74°C to 91°C.

Given that the software only does a thermodynamic analysis of the alloy, not considering the kinetic side of transformations, the temperature at which it starts calculating does not influences the results. Specifically, by looking at the charts presented before [Tab.2.3; Tab.2.7], it is clear that if the starting temperature is above 631,3°C the results remain unchanged, otherwise some datas will be missing (e.g. formation temperature of some compounds).

Chapter 3

Sample preparation

3.1 Material preparation

The material used, as anticipated above, is alloy EN-46000. Following, are presented both the low-Fe alloy and the high-Fe alloy Fe wt.% :

Tab. 3.1: Low-Fe Alloy and High-Fe alloy iron contents in wt.%

EN AB 46000	
Low-Fe Alloy	0,772 wt.% Fe
High-Fe Alloy	1,2 % wt.% Fe

Once the correct components are selected, the various sprue are weighted in order to gather the correct amount of material. Since the samples obtained by the castings weigh about 116g and seven of these will be produced, 1.5 kg of material is inserted in the crucible to be sure that enough material will be melted. Subsequently, the die used for the pours needs cleaning too, since release agents such as boron nitride alumina or silica were previously applied to it. The release agents are usually used to make the sample removal easier. The downside of these agents is that, since they have a ceramic basis, they tend to form a thermal barrier, which is not wanted since a rapid cooling is required in this experiment. Therefore, the chemicals are removed and dry molding is done. If dry casting causes any problem, a possible solution is to use graphite as a release agent which does not create a thermal barrier since it is really conductive and not chemically reactive to Al. Nevertheless, its addition will not be

necessary because the alloy is rich in Fe, thus welding of the sample to the die will not happen.
Moreover, the die needs further cleaning to remove the Fe oxide, or calamine.

***Fig. 3.1**: The cleaned die used for the casting process*

3.2 Casting

First things first the temperatures at which the furnace will be set are defined as described in the chart [Tab. 3.2]. The first temperature of the furnace (680°C) is set and then keeps such temperature until the end of the first casting. The furnace used is shown in the following image [Fig. 3.2]:

Fig. 3.2: The furnace used to heat the material

The temperature recorded by the furnace is the one detected by the thermocouples on the top of the oven, so it is necessary to maintain the temperature of the furnace to equalize the temperature of the material inside it, in particular crucible, hence the alloy.

Tab 3.2: *Temperatures at which the various samples are casted*

CASTING NUMBER	CASTING TEMPERATURE (±5°C)
1	680
2	750
3	820
4	890
5	960
6	1030

The die is preheated to 150°C for a few minutes to eliminate the humidity trapped inside it to stop the metal from spurting. [Fig. 3.3]

Fig. 3.3*: The preheat furnace used to dehumidify the die*

The crucible is then removed from the furnace and skimmed thoroughly with a slotted spoon, this is done to eliminate the Al oxide that covers the bath surface, where the sludge nucleates. Then, it is inserted back in the furnace for another 20 minutes. Now the small amount of slag formed, during the last furnace use, is rapidly removed to avoid the melt to cool down and then it is poured into the die. The sample obtained is first cooled down in air and then in water. After that, the crucible is reinserted in the furnace which temperature is now turned up to the next one, previously defined. The metal is held inside the furnace for about 40 minutes, enough for the furnace to reach the correct temperature and for the whole alloy to reach the temperature as well. Then the process just described above is repeated for every casting.

Fig. 3.4*: One of the samples obtained by the casting process*

The time requested for the furnace to reach the subsequent temperature is presented is the following chart:

Tab. 3.3: Time requested for the furnace to reach the subsequent temperature and furnace heating rate

	680 - 750°C	750 - 820°C	820 - 890°C	890 - 960°C	960 - 1030°C
Time (low Fe)	3min 58s	4min 46s	4min 57s	6min 23s	7min 03s
Heating Rate (low Fe) [°C/s]	0.294	0.244	0.236	0.183	0.165
Time (high Fe)	4min 28s	4min 52s	5min 41s	7min 07s	7min 48s
Heating Rate (high Fe)[°C/s]	0.261	0.239	0.205	0.163	0.150

Larger amounts of slag are detected as the temperature increases, although these differences are negligible; also, as temperature raises, the alloys seethe more because of higher hydrogen presence since its solubility increases with temperature.

3.3 Sample processing

The samples are weighted [Tab. 3.4] and engraved in order to recognize them throughout the experiment.

Tab. 3.4: Weight of each sample after the solidification process

Sample	**1**	**2**	**3**	**4**	**5**	**6**	**7**
Casting temperature (±5°C)	680°C	750°C	820°C	890°C	960°C	1030°C	1100°C
Weight (low Fe)	102g	104,91g	115,48g	104,74g	100,26g	123,04g	121,67g
Weight (high Fe)	113g	111.5g	117g	127g	117g	111g	111g

Two pieces are cut from the same sample to use one of them for the wear test and the other one for the metallographic test; the face analyzed needs to be the one that the two sections share. To do so, 25 mm from the bottom of the sample are marked: this part of the sample is the one that will be used for the tests. Then two different marks are made 10 mm away from the 25mm mark [Fig 3.5].

***Fig 3.5**: Length at which the samples are marked (25 mm)*

The sample is cut on the marks just described. The cutting machine [Fig. 3.6] utilized for this experiment uses water and lubricant to avoid wear and overheating of both the grinding wheel and the samples.

***Fig. 3.6**: Cutting machine used for material preparation*

The two pieces obtained with the last step are now filed with a lapping machine [Fig.3.7] to remove any present burr. Specifically, the machine is set to 180 rpm and the sanding paper used has a granulometry of 180 (P180).

Fig. 3.7: Lapping machines used to polish and roughing the samples

Once the new samples are properly filed, the next step is using the embedding machine [Fig. 3.8] to incorporate the small alloy cylinders into a resin. The samples are inserted with the face of interest facing down; then the resin is added. The machine is set to go up to 170°C with pressure of 180bar; once the conditions are reached the machine keeps them for 7min 30s and then cools down to room temperature in 4 minutes. During the cooling process high pressures are kept inside the machine to prevent gaps between the sample and the resin.

Fig. 3.8: Embedding machine used to incorporate the alloy into the resin

The lapping machine is used again, specifically with subsequent sanding papers P180, P600, P1200, P2400 and then diamond paste cloth of 6 micron; all samples are processed as described, while only the samples that will undergo the metallographic test are also worked with colloidal silica to abrade, polish and flatten out the surface. Two different suspensions can be used for this part of the process: UPS or UPU; UPS has chemical agents inside it, UPU does not, therefore this last is used to not spoil the samples' surface. The material has to be polished up to mirror-like conditions in order to obtain a better vision with the microscope.

Chapter 4

Tests and data analysis

4.1 Metallographic analysis

The samples polished with the colloidal silica are used for the metallographic analysis. For this test a Leica DAS Mikroskop LEITZ DMR microscope with different enlargements of 25x-50x-100x-250x-500x is used.

The goal of this test is to analyze the material microstructure and the SDAS [Fig. 4.1] [Tab 4.1], i.e. the distance between the secondary aluminium dendrites arms, of all samples. The SDAS is scanned to determine whether the cooling rate is the same on every cast.

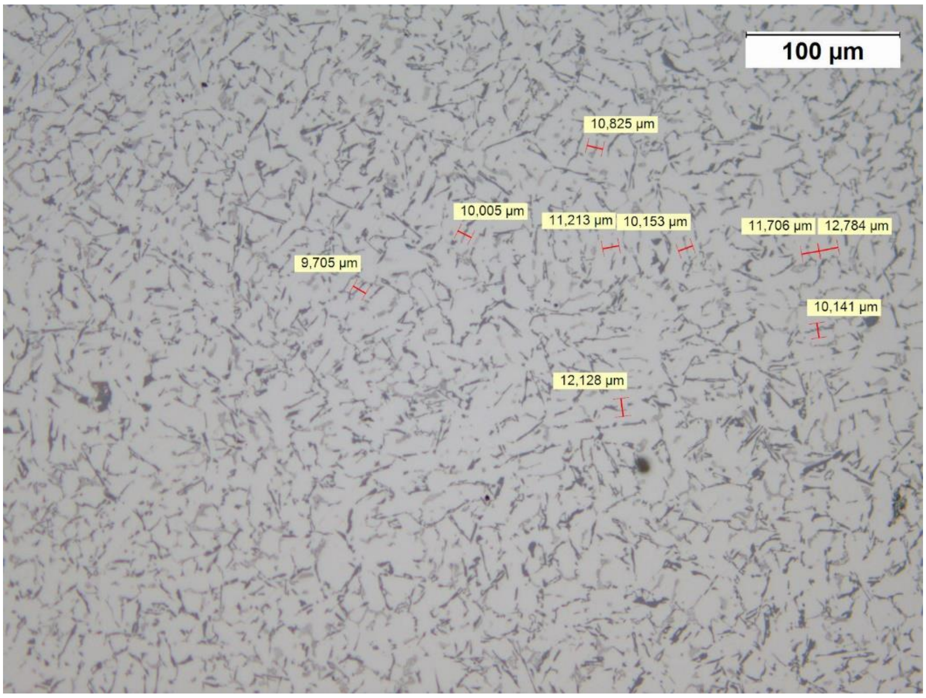

Fig. 4.1*: SDAS on the sample with low-Fe wt.% casted at 1030°C*

***Tab. 4.1**: Total SDAS of all samples*

LOW-Fe ALLOY		HIGH-Fe ALLOY	
Temperature [°C]	SDAS [µm]	Temperature [°C]	SDAS [µm]
680	11,3 ± 1,5	680	10,4±0,8
750	11 ± 1	750	10±1
820	10,5 ± 1	820	10±1
890	10,9 ± 0,6	890	9,9±0,3
960	10 ± 1	960	9,8±0,3
1030	10,8 ± 0,4	1030	10±1

4.2 Acid etching and iron-analysis

The samples are etched with an 80% water and 20% sulfuric acid solution. The mixture is prepared inside a graduated cylinder and then poured into a becker. Hence, using an electric stove the acid is heated at a temperature of 70 °C.

As soon as the correct temperature is reached, the becker is removed from the electric stove and placed on a room temperature plan; here, the sample is totally immersed in the solution for about 1 minute and 20 seconds. Then it is rinsed with water and allowed to cool.

To analyse the samples an optic microscope is used (Leica DAS Mikroskop LEITZ DMR), where it is observed that the Fe-rich compounds assumed a blackish colour that made them stand out from the rest of the matrix. In Fig. 4.2 is better shown the result of the chemical attack.

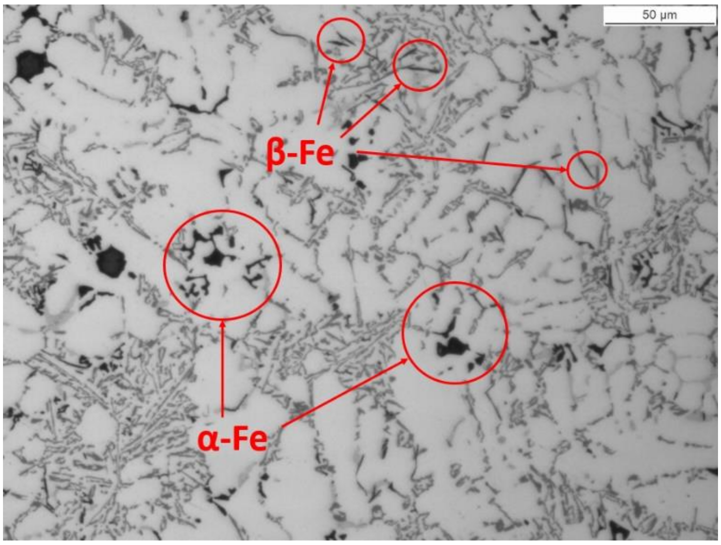

Fig. 4.2: The high-Fe sample casted at 680°C after the chemical etching

Subsequently, 9 images for each sample are acquired forming a square, at a 200x magnification. [Fig. 4.3]

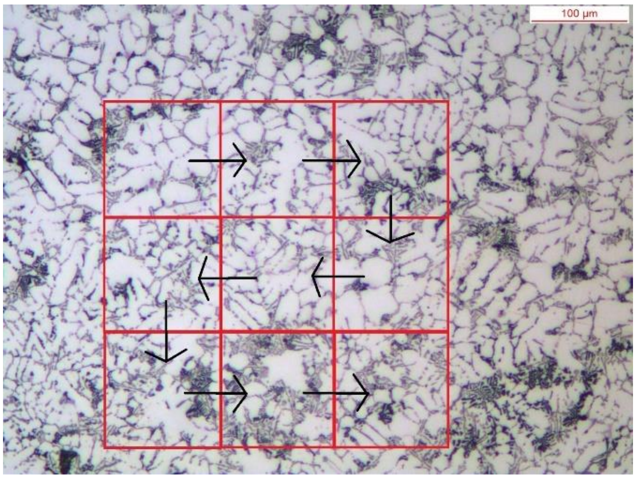

Fig. 4.3: How the subsequently images are taken

Then, using the software in these specific images, it is possible to determine the quantity of Fe-rich compounds in relation to the whole matrix. Subsequently, highlighting β-phase characteristics needles, it is quantified as the percentage of β-iron compared to the total percentage of Fe-rich compounds.

The morphological evolution of the structure led from temperature is represented in the Tab. 4.2:

Low wt.%Fe Alloy - Center of the sample	High wt.%Fe Alloy - Center of the sample

Low wt.%Fe - 680 °C	High wt.%Fe - 680 °C
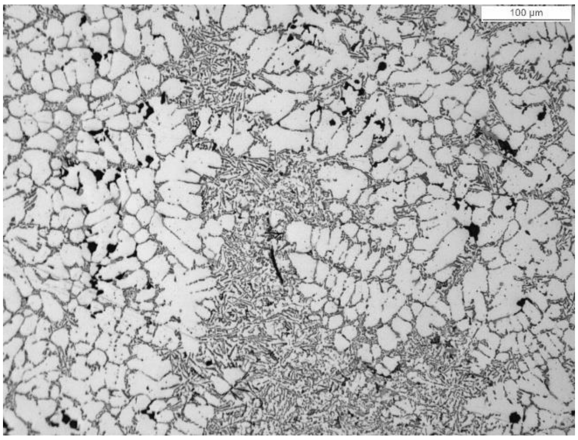	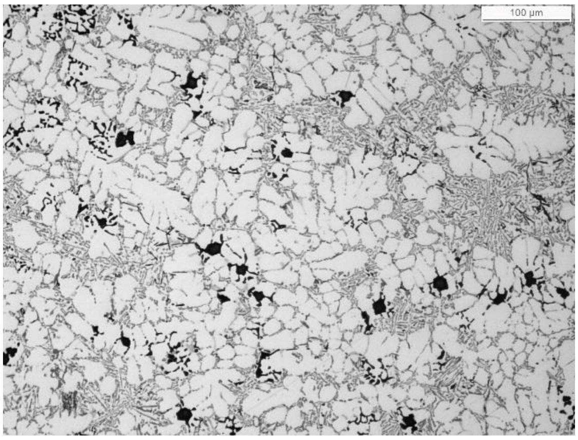
Low wt.%Fe - 750°C	High wt.%Fe - 750 °C
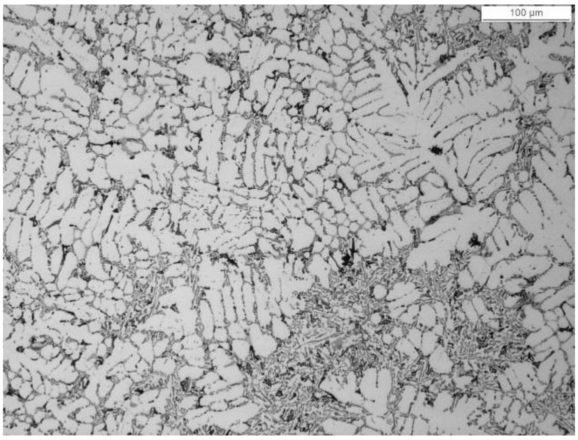	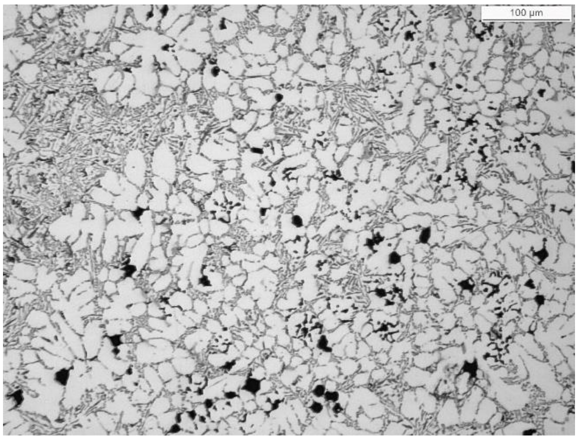
Low wt.%Fe - 820 °C	High wt.%Fe - 820 °C
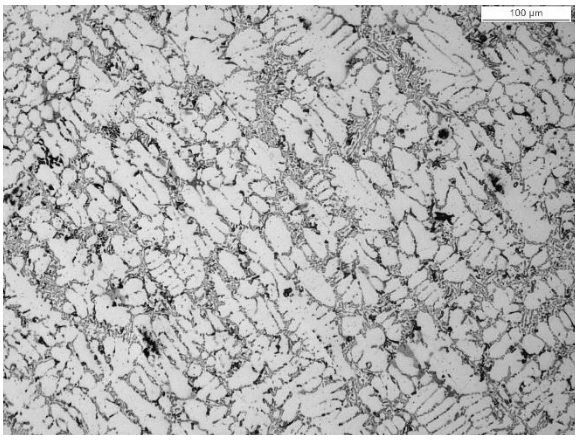	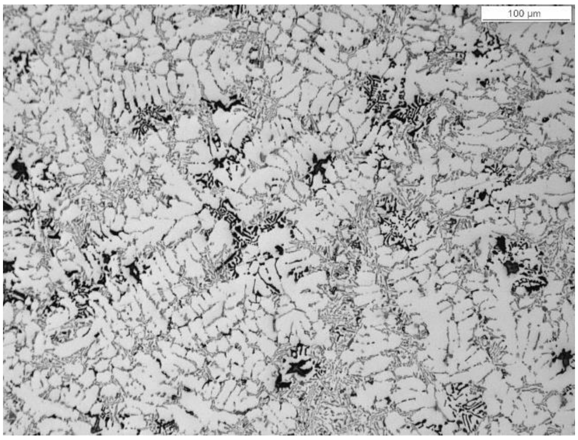

Low wt.%Fe - 890 °C	High wt.%Fe - 890 °C
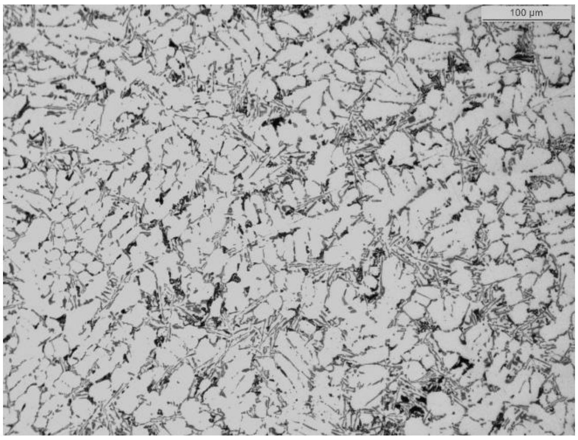	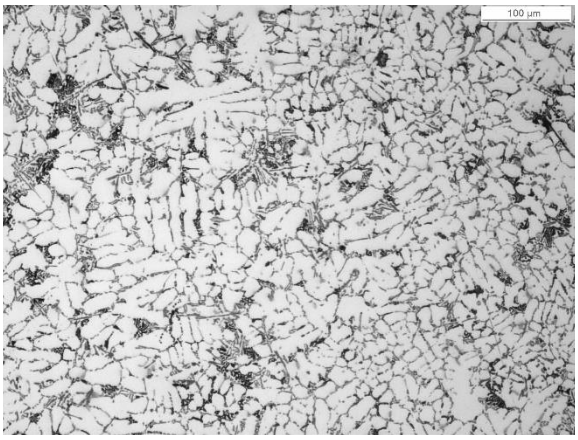
Low wt.%Fe - 960 °C	High wt.%Fe - 960 °C
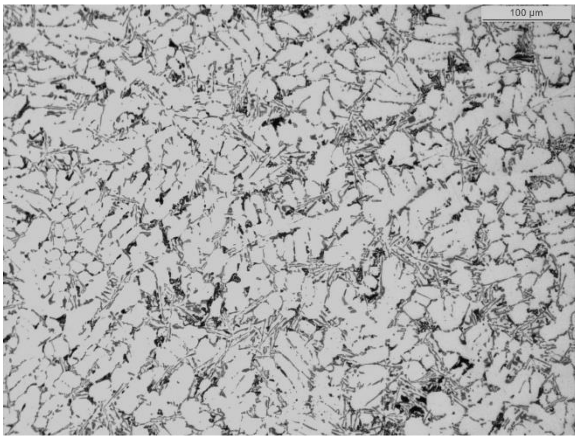	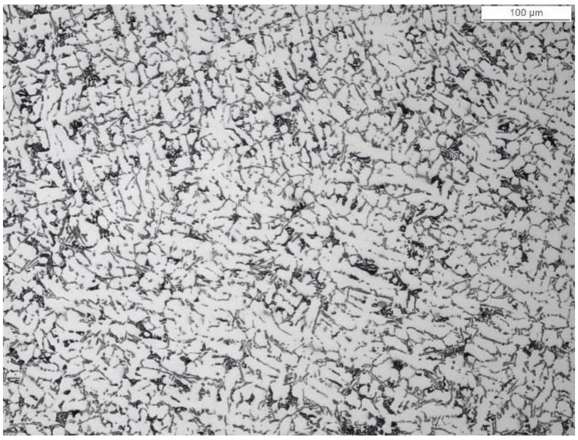
Low wt.%Fe - 1030 °C	High wt.%Fe - 1030 °C
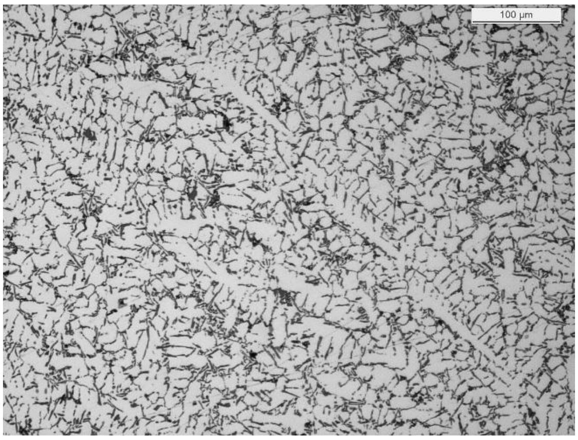	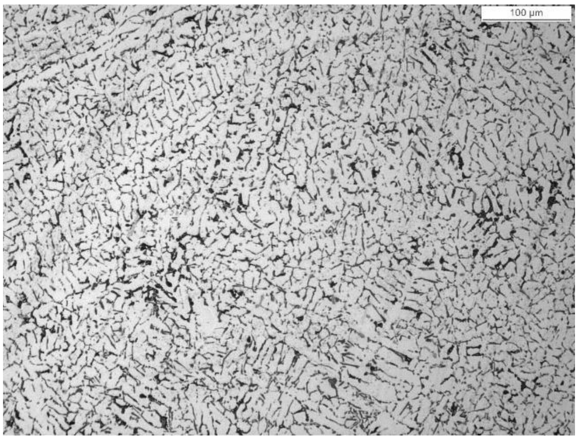

Tab. 4.2: *Comparison between the two alloys analyzed with different casting temperatures*

4.2.1 Considerations

Raising the bath temperature, it is noticed that the percentage of β-phase, compared to the percentage of the others iron compounds, decreases. In particular, in the lower Fe alloy, from 820 °C no more β-phase needles are detected, instead, in the other alloy, the presence of acicular form is still spotted at 890°C.

The amount of the β-phase is generally higher in the high-Fe alloy. In fact, analysing the data, it is noticed that the percentage of β-phase in the low-Fe alloy casted at 680°C is lower than the amount in the high-Fe alloy sample casted at 820 °C.

Thanks to these considerations, it is deduced how for the first steps of the superheating bath, the increase of Fe wt.% from 0.722% up to 1.223% has a high impact on the quantity of Fe β-phase formed in the considered alloy.

Another factor that seems to be influenced by the temperature variation is the morphology of α-Fe. In fact, up to 750 °C α-Fe can mainly be found as polyhedral structure and, in low quantities, as Chinese-script form.

Instead, starting from 820°C, the Chinese-script structure begins to be predominantly, while the polyhedral one becomes very small and difficult to detect.

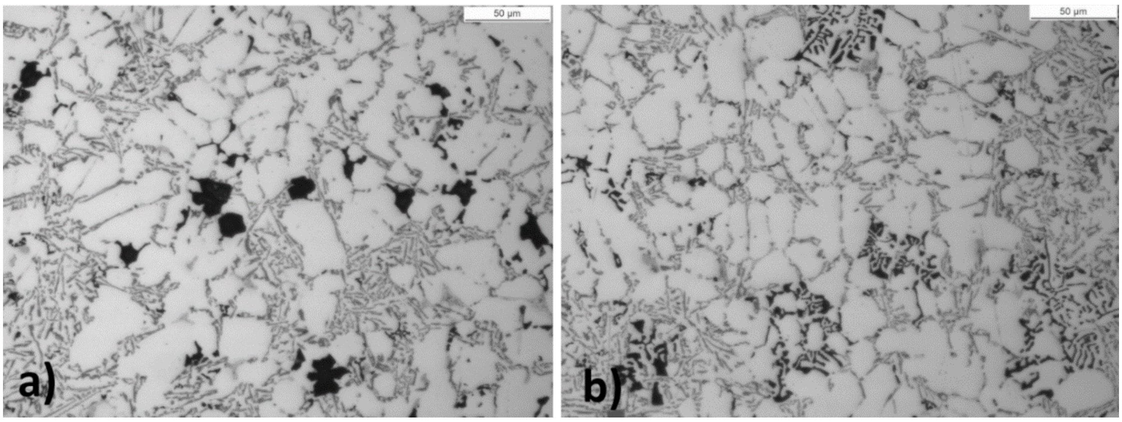

Fig. 4.4: Microstructure of samples after the acid etching. (a) High Fe alloy at melting temperature of 750°C , (b) High Fe alloy at melting temperature of 820°C

Moreover, by increasing the temperature, the entire structure tends to refine, as shown in [Fig 4.5], where the two alloys are compared for two different casting temperatures.

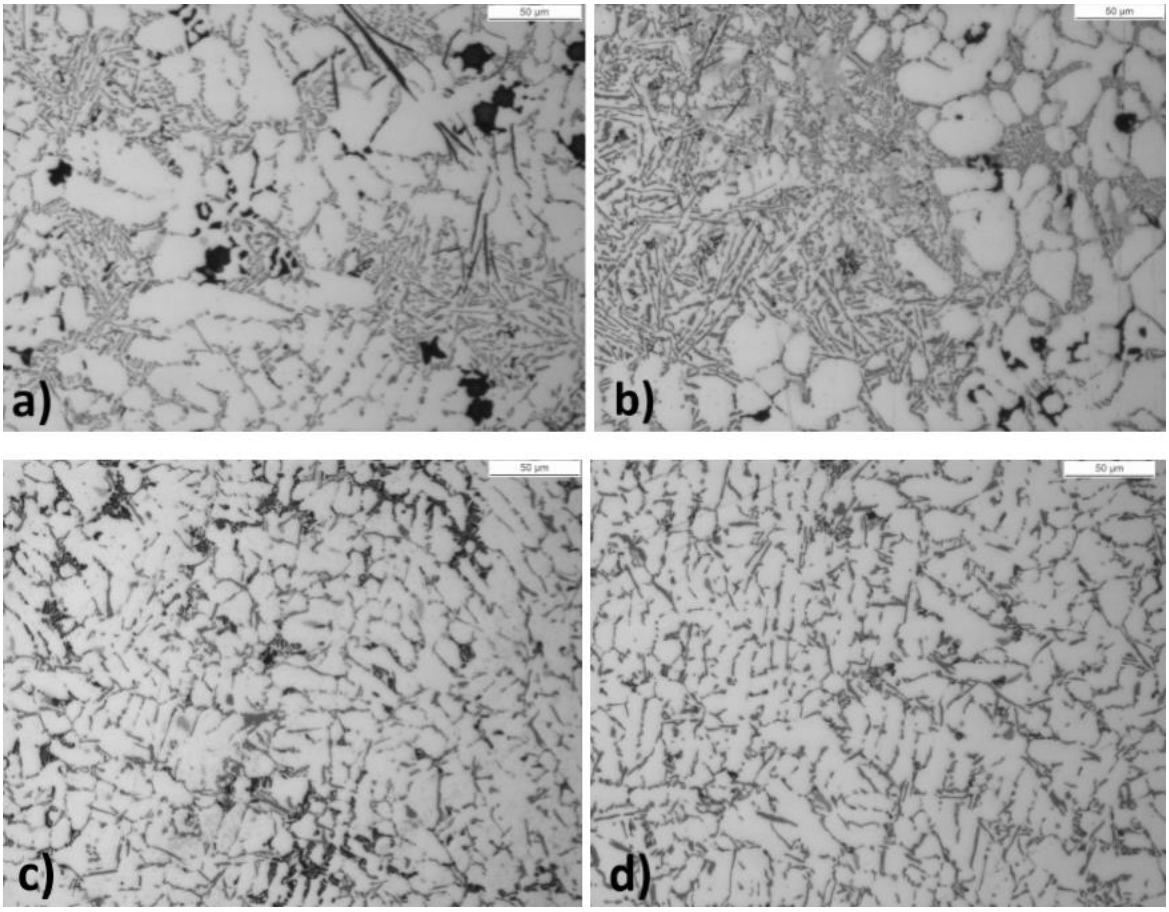

Fig. 4.5*: Microstructure of samples after the acid etching. (a) High-Fe alloy at melting temperature of 680°C, (b) Low-Fe alloy at melting temperature of 680°C, (c) High-Fe alloy at melting temperature of 1030°C, (d) Low-Fe alloy at melting temperature of 1030°C*

4.3 Minitab analysis

Working on the data obtained by the metallographic analysis, by using minitab, it is possible to plot several graphs that are described below.

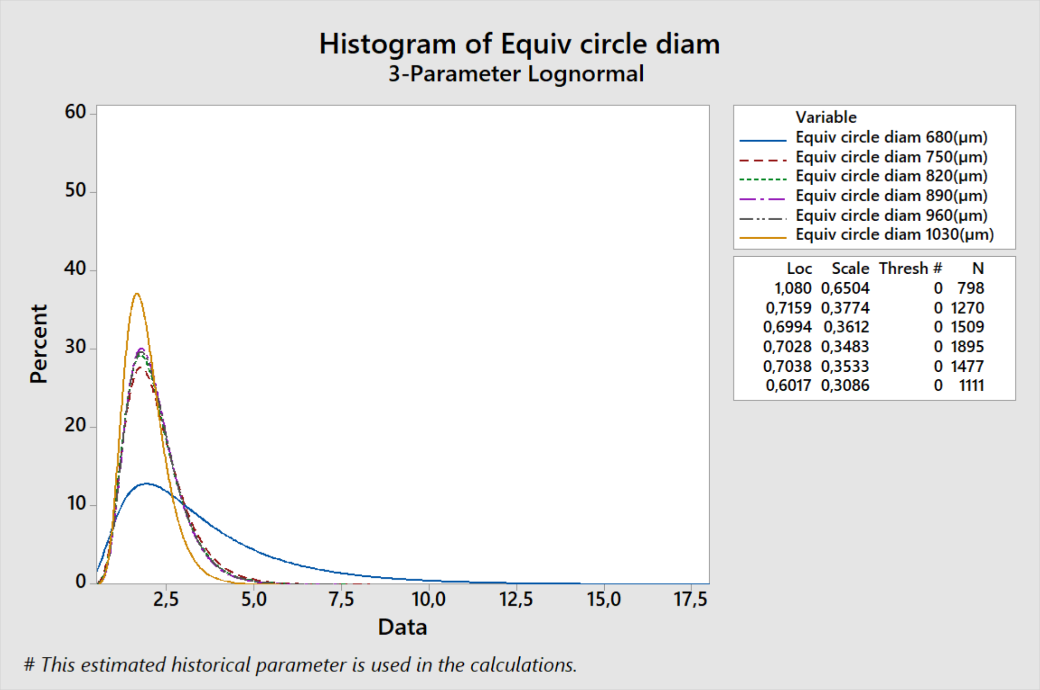

***Fig. 4.6**: Percentage amount of Fe-rich particles with a specific equivalent circle diameter for the low-Fe alloy*

The equivalent circle diameter is the diameter of a circle with the same area of the particle. Regarding the equivalent circle diameter graphs, from Fig. 4.6, is shown the percentage amount of the Fe-rich compounds that assume a determined equivalent circle diameter value, as function of the area value (in the low-Fe alloy). Regarding the equivalent circle diameter graphs, it is noticed that, for temperatures higher than 680°C, finer compounds substantially increase in percentage. Instead, in the 750-960°C casting temperature gap, their value remains almost constant. Furthermore, the quantity of finer compounds rises again at a casting temperature of 1030°C. So, considering the data defined, is possible to say that to obtain fine Fe-rich compounds it is unnecessary to superheat the bath at a temperature of 1030°C. Even though the quantity of compound with a small equivalent circle diameter remains constant at the casting temperatures between 750°C and 960°C, at 750°C β-phase is still detected with a 0,011 wt.%. Hence, from a performance and economical point of view, for the Low-Fe alloy would be optimal to cast at a temperature between 820°C and 960°C to have the best compromise among Fe-rich compounds size, absence of β-phase and energy consumption related to the furnace where the alloy is casted.

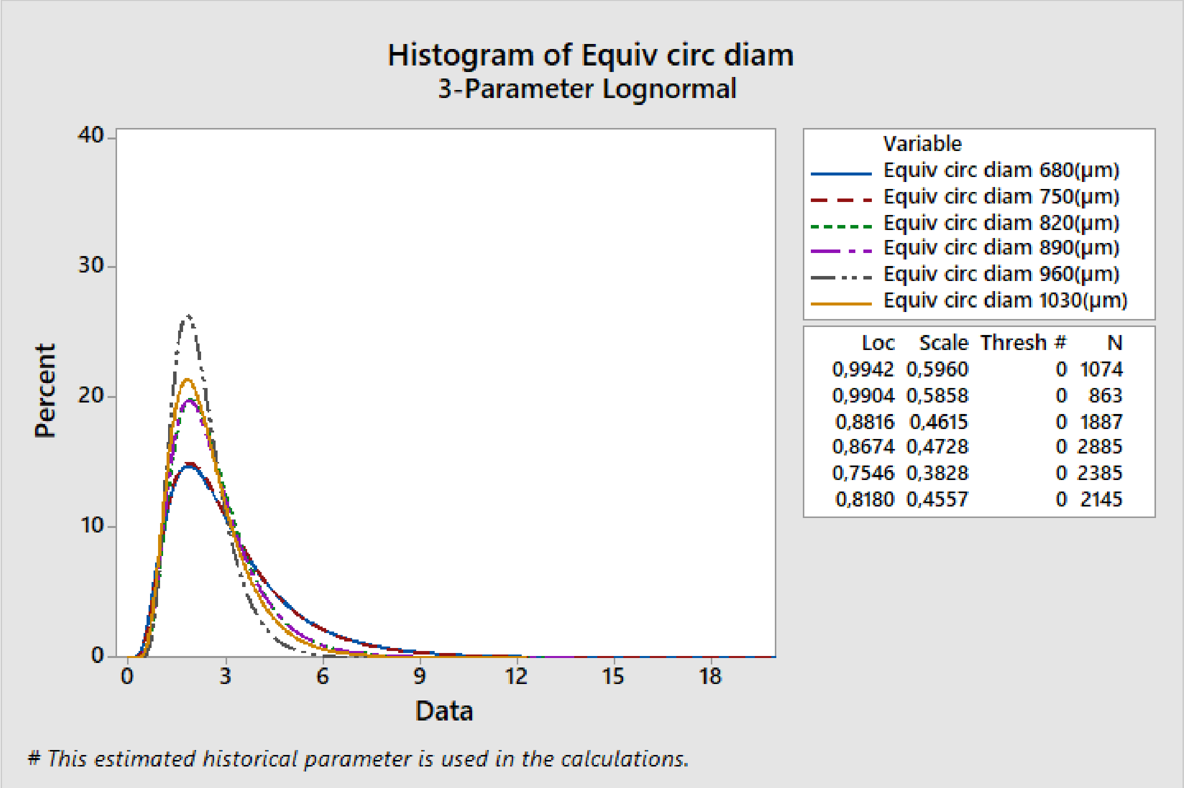

Histogram of Equiv circ diam

3-Parameter Lognormal

Loc	Scale	Thresh #	N
0,9942	0,5960	0	1074
0,9904	0,5858	0	863
0,8816	0,4615	0	1887
0,8674	0,4728	0	2885
0,7546	0,3828	0	2385
0,8180	0,4557	0	2145

 # This estimated historical parameter is used in the calculations.

Fig. 4.7: Percentage amount of Fe-rich particles with a specific equivalent circle diameter for the High-Fe alloy

Regarding the High-Fe alloy [Fig. 4.7], it is shown that as the temperature increases the percentage increase of the Fe-rich compounds of small dimensions is not significant. This is due to the fact that the higher Fe wt.% promotes the formation of bigger compounds rather than small ones.

Furthermore, as shown in the Low-Fe alloy, it is noted that the β-Fe compounds presence is not highly marked at casting temperatures higher than 750°C (0,049 wt.%). Therefore, as stated above for the other alloy, such temperature is sufficient to avoid the formation of β-Fe, thus it is not necessary to use elevated casting temperatures.

To underline what said before, the higher refinement gap of Fe-rich compounds, in Low-Fe alloy, obtained from a casting temperature of 680°C up to 750°C, is shown in Fig. 4.8; the average equivalent circle diameter, for temperatures higher than 750°C, remains roughly constant. In the High-Fe alloy the average equivalent circle diameter difference between the different casting temperatures is less marked.

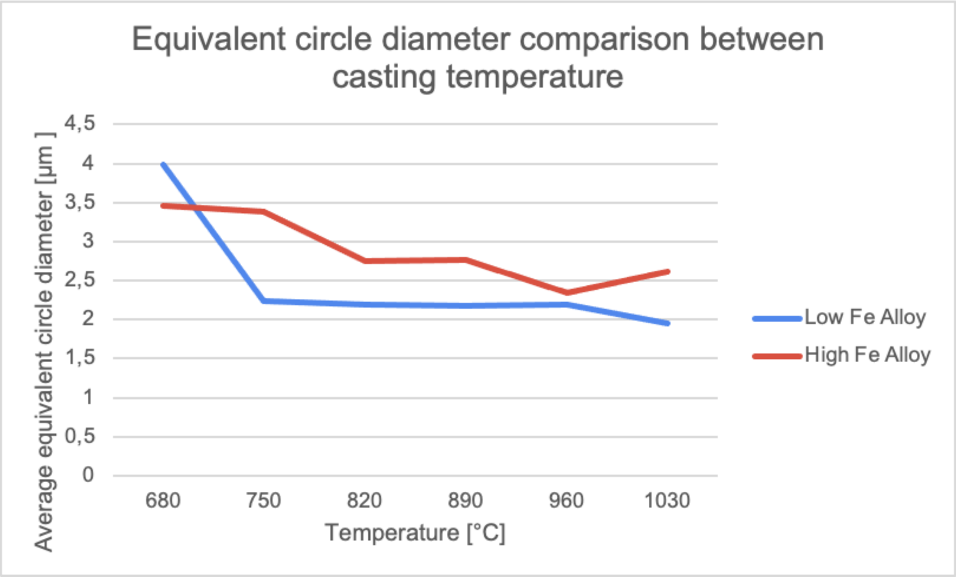

Fig. 4.8: The average equivalent circle diameter of the Fe-rich compounds as function of the casting temperatures

Economically speaking, it is interesting to observe how the most marked refining of the Fe-rich compounds in the High-Fe alloy is obtained with a casting temperature of 960°C. At this temperature, an approximate decrementation of 70 % of the average equivalent circle diameter is reached, such dimension, as shown in the chart above, can be obtained in the Low-Fe alloy with a casting temperature of only 750°C, much lower than the one just mentioned.

Regarding the High-Fe alloy, looking at the graphs obtained for the perimeter and the equivalent circle diameter, a minimum value could be noticed in correspondence of 960°C. This means that at this temperature, the Fe-rich compounds are on average smaller than at all other temperatures. For what concerns the Low-Fe alloy, in confirmation of what is stated for the equivalent circle diameter graph, the highest gap in level of refinement is noticed between the casting temperatures of 680°C and 750°C. Moreover, the lowest value of both the equivalent circle diameter and the average perimeter is observed at the casting temperature of 1030°C for the Low-Fe alloy. [Fig. 4.9]

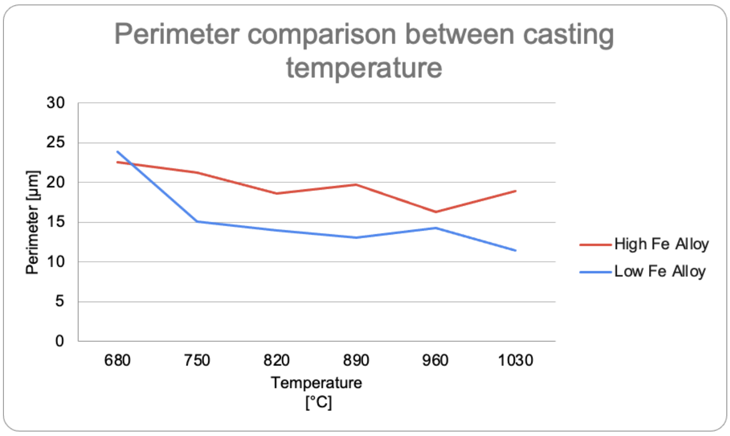

***Fig. 4.9**: The perimeter of the Fe particles of the two alloys as function of the casting temperatures*

To support this data for the High-Fe alloy, three images taken from the acid etching for each temperature are reported [Tab. 4.3]:

890 °C	960 °C	1030 °C
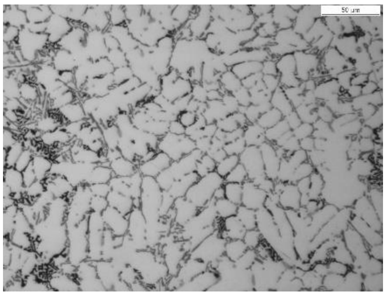	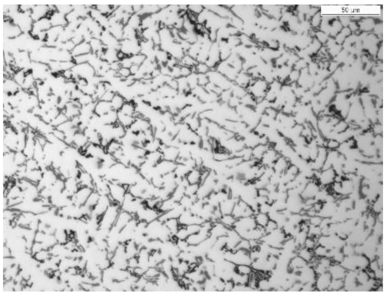	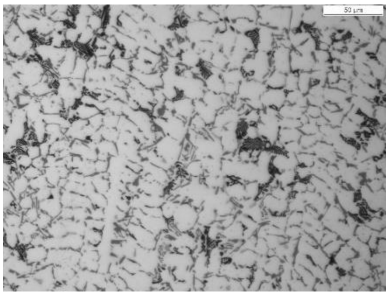
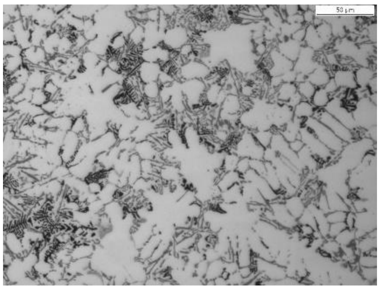	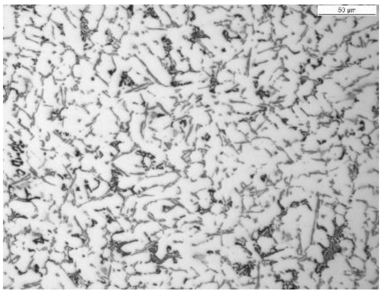	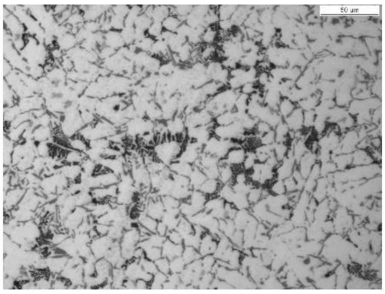
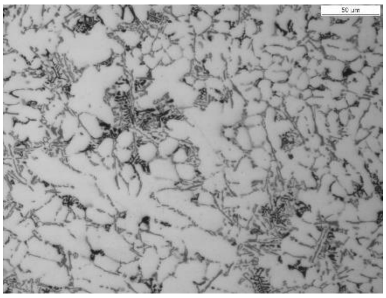	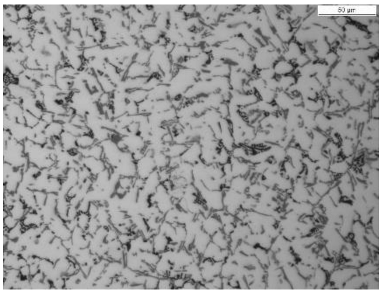	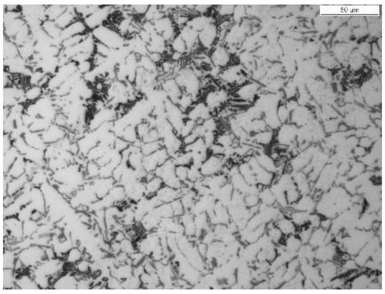

***Tab. 4.3**: Micrographs taken from the acid etching at three different temperature(890°C, 960°C, 1030°C)*

From the comparison between the images taken at 890 °C and 1030 °C it is observed that at both temperatures, Fe-rich compounds are worse distributed and more concentrated in specific areas of the material. Meanwhile, at a casting temperature of 960 °C, the distribution is much more homogeneous. Analyzing the other graphs given by the software, the Low-Fe alloy has a higher value of width at 680°C, while the presence of β leads to a higher value of length on the High-Fe alloy which is deleterious for mechanical properties. These alloys present a major refinement by increasing the temperature, indeed the width and the length [Fig. 4.10] tends to decrease at higher temperatures. In the Low-Fe alloy these parameters remain the same from 750°C to 960°C, this fact is related to a lower percentage of β, which has an acicular form, while the Fe-rich compounds, which have a polyhedral or chinese forms, are more compact than β particles. [Fig. 4.5]

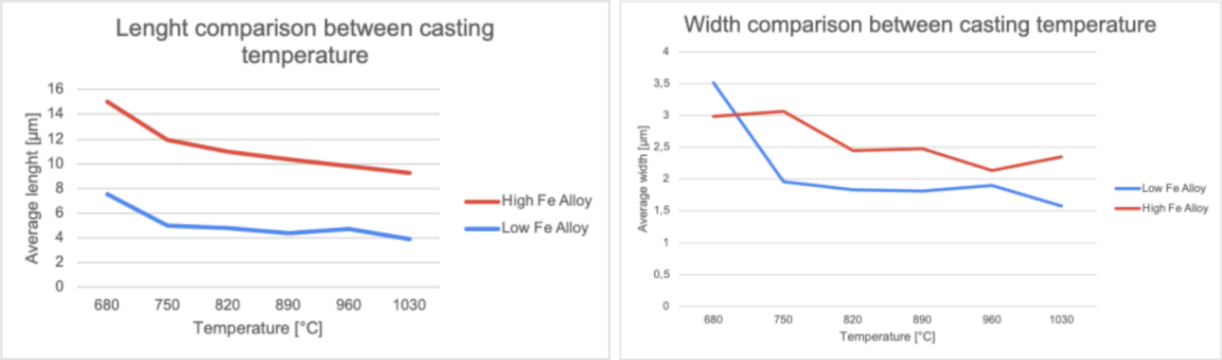

***Fig. 4.10**: Graphs of length and width of the Fe particles as function of the casting temperatures*

The roundness contributes to the morphological definition of the compounds and it is automatically calculated by the software.

The Fig. 4.11 shows different trends for the alloys: the high-Fe alloy exhibits a roundness increasing as temperature increases, on the other hand, in the low-Fe alloy, generally, an opposite development is shown.

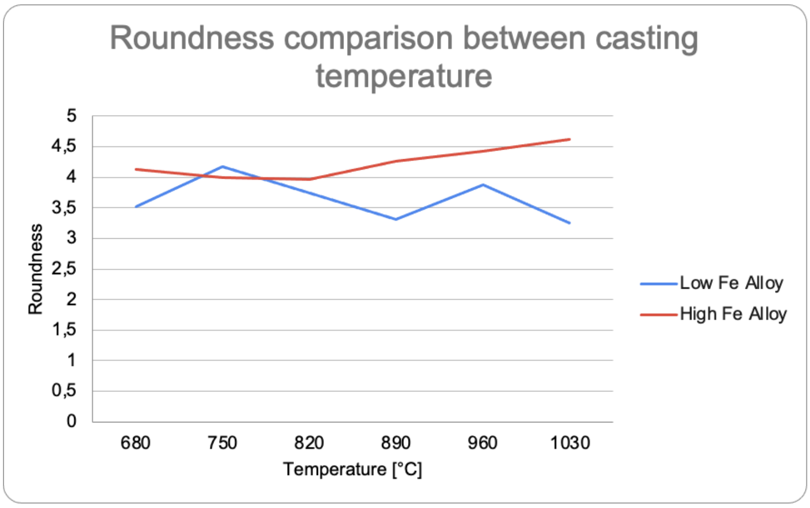

Fig 4.11*: The roundness of Fe particles as function of the casting temperatures*

For the high-Fe alloy, the aspect ratio presents a slow decrease at higher temperatures, meanwhile the low-Fe alloy tends to have a constant value as temperature increases, therefore the aspect ratio is not modified by temperature. [Fig. 4.12]

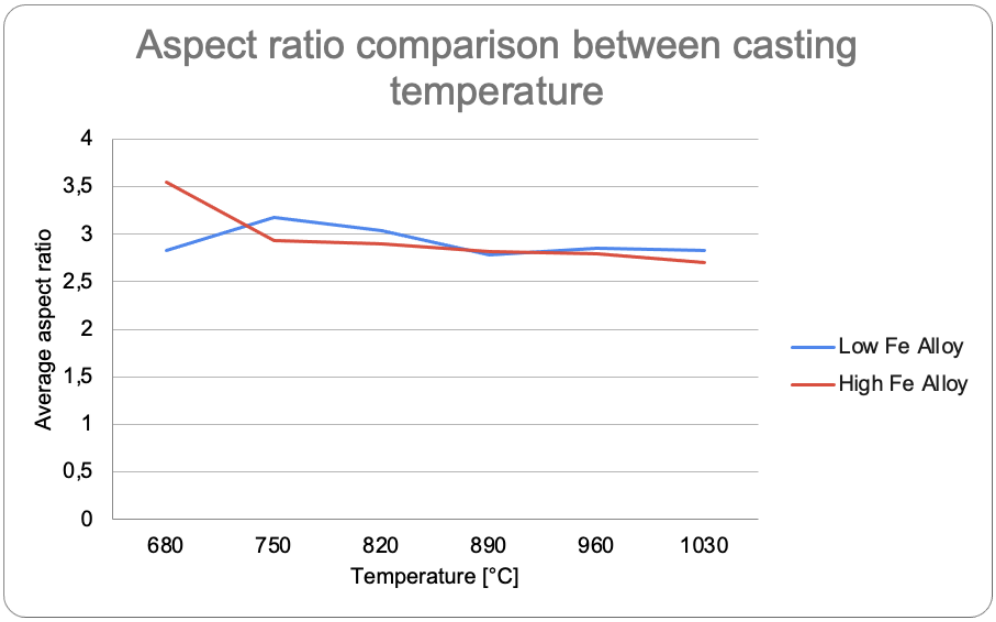

Fig. 4.12*: The aspect ratio of the Fe-rich compounds as function of the casting temperatures*

4.4 Hardness test

A Brinell test is done to quantify the material hardness. The durometer used [Fig 4.13] presents a spherical indenter of 2.5mm diameter made of tungsten carbide and a load of 62,5 kg is used.

Fig 4.13*: The durometer used for the hardness test*

The first thing to do is to check whether the sample surface is flat; if not, the values obtained by the test are unreliable. Once the flatness is confirmed, the test starts: the load is applied to the sample for a total of 15s, as defined by the standard ISO-6506-1. The print that is formed is now analyzed with a dedicated lens located on the machine. [Fig. 4.14]

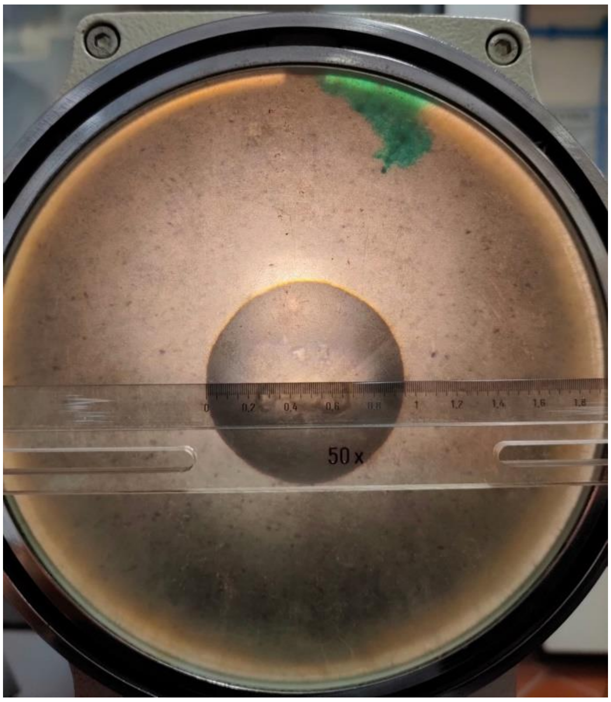

***Fig. 4.14**: The print formed on the sample after the hardness test seen through the lens*

Two perpendicular diameters of the print are considered and an average of the two is calculated. It is now necessary to verify whether the correct load has been used for the specific material; to do so the following formula is used:

$$\frac{print\ average\ diameter}{indenter\ diameter}$$

The value obtained must be between 0.24 and 0.6 (ISO-6506-1), otherwise the load needs to be changed. For this examination, the result is 0.36, therefore the test has been set correctly. Afterwards, the regulated standard table is consulted and the material hardness value is obtained based on the average diameter and the load utilized. The test is repeated three times for each sample. Each indentation is as far from the others as four times the print diameter; by doing so, the test repetitions do not influence each other.

The obtained results are resumed in Tab. 4.4

Tab. 4.4*: The values obtained from the hardness test [HB] with the standard deviation for both the alloys at different casting temperatures*

Casting temperature	HB Low wt.%Fe	St. Dev.	HB High wt.%Fe	St. Dev.
680	90	1	89	2
750	92	2	90	2
820	95	1	90	1
890	95	1	90	2
960	96	2	92	2
1030	97	1	95	2

The highest values of standard deviation calculated on the data obtained by the hardness tests are around 2 Brinell points. That corresponds to an error of about 2% of the total hardness values.

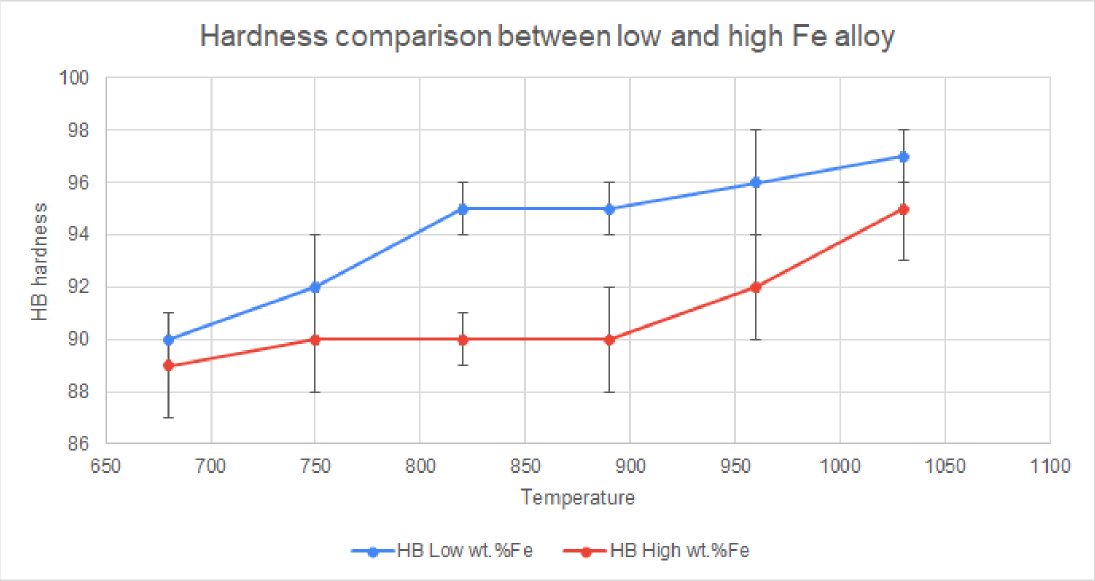

Fig. 4.15*: Hardness comparison*

Generally speaking, as the bath temperature rises, both of the alloys present an increase in hardness.

It is also quite surprising to notice that the low-Fe alloy is always harder than the high-Fe alloy. Hence, it is possible to say that the bath temperature has a greater contribution to the alloy's hardness rather than its iron content.

Specifically, the low-Fe alloy presents a hardness enhancement of 7,78%, while the high-Fe alloy shows an increase of 6,74%. Taking into account the standard deviations, it can be stated that the Fe wt.% difference between the alloys seems to not be influencing significantly the hardness increase.

Analysing the path of hardness increase in the alloys in between the temperatures 680°C and 1030°C, it is evident that the augmentation is different for the two alloys: the low-Fe alloy hardness increase can be approximated to a linear trend between 680°C and 820°C. Subsequently, a narrow plateau is shown up to 890°C, followed by a secondary linear enhancement with a lower gradient than the initial part.

The high-Fe alloy shows a long plateau up to 890 °C, therefore the hardness improvement is significant only for casting temperatures higher than 890°C, where hardness increases with a linear trend up to 1030°C.

4.4.1 Considerations

Regarding the regulation UNI-EN 1676 and 1706 [19] the hardness range for the alloys analysed (EN 46000) is 80HB-120HB, therefore even a 7HB increment is significant for the alloy performances. Hence, the casting temperature 820°C and the low-Fe alloys is the best compromise between hardness and economical advantage, since the augmentation is of 5HB with an increase of only 140°C. Specifically, at 820°C the hardness value for the low-Fe alloy is higher than every value found in the high-Fe alloy.

Considering the progression of the morphological refinement, which increases along with the casting temperature [Tab. 4.2], it is deduced that the long initial plateau(680°C-890°C) in the high-Fe alloy [Fig. 4.16] is due to the presence of coarse grain. Moreover, in accordance with the Hall Petch equation, the yield stress increases when a significant grain refinement presents, which happens from 960°C and up. Since the yield stress is directly proportional to hardness, this last one increases too.

Regarding the low-Fe alloy, again referring to [Fig. 4.16], from 680°C to 820°C the progressive hardness increase corresponds to the grain refinement observed; moreover, between 820 °C and 890 °C, the hardness plateau is correlated to the grain size, which in fact remains constant [Tab. 4.2]. Afterwards, a linear increment of hardness is detected, linked to the continuous refinement of the grain up to 1030 °C.

Referring to the hardness tests results, the fact that the low-Fe alloy is harder than the high-Fe one finds a reason in literature; in fact, according to [14], an increment of the iron content leads to an increase of porosities formed during the last step of solidification. Hence, it is possible that this factor influences the measurements, providing a decrement of the hardness. To reduce the amount of porosities in the high iron alloy down to the same amount found in the low-Fe alloy, an addition of 0.5% up to 1% of Mn is sufficient.

Moreover, supersaturation of the Al phase and the size of precipitates and content of pre-dendritic Al15(Fe,Mn)3Si2 significantly influence the alloys' mechanical properties. Specifically, at 750°C the precipitates are smaller and create coherent boundaries leading to high levels of hardness in the low iron alloy. In the high iron alloy instead, the precipitates that form have larger dimension and form semi-coherent boundaries, resulting in lower hardness levels.

4.5 Wear test

A tribometer is used for the wear resistance test. [Fig. 4.16]:

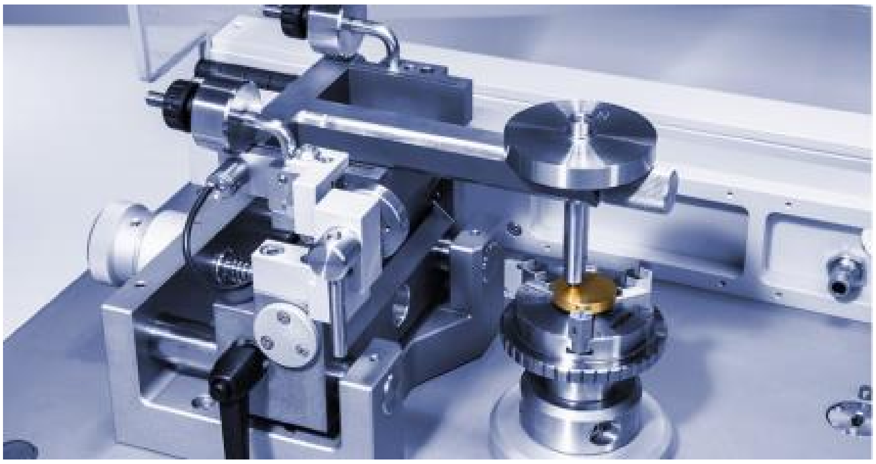

***Fig. 4.16**: The tribometer used for the wear test [20]*

First, it is verified that all the samples are plain in order to obtain more specific results. To do so, a comparator [Fig. 4.17] is fixed to the tribometer arm and it is lowered so that the pin touches the sample's head. The maximum accepted tolerance value for planarity is 0.05 mm. From now on the sample is handled only with gloves on because any possible grease residue could negatively change its weight.

***Fig. 4.17**: The comparator used to verify the planarity of the samples before the wear test [21]*

Subsequently, the samples are weighted with an electronic scale with a precision of 0.0001 g. Because of such precision, the measurements could change day by day, therefore a calibration sample is prepared so that all the weighings done on different days and/or conditions match. The weighing is repeated at least three times per sample to be as specific as possible. Once the sample is weighed, it undergoes the wear resistance test. The machine is set with a load of 1N, a linear speed of 6.3 cm/s for 24000 rounds total and a 4 mm radius, obtaining a total travelled distance of 603,487m. The pin used to wear the component is an alumina (Al_2O_3) sphere with a 6 mm diameter. An airflow of 0.1 bar is positioned onto the surface to remove any possible debris that forms, which could influence the final results. Once the test is over, after about 2h 40min, the sample is weighed again. The different weights, before and after the test, represent the amount of material that has been removed from the sample and suggests its wear resistance. For better comprehensions of the derived data, such values are normalized into $\frac{\mathrm{mm}^3}{\mathrm{m\,N\,10^{-3}}}$ with the formula (1). In accordance with article [15], the material average density is approximated to 2,770 $\frac{\mathrm{g}}{\mathrm{cm}^3}$

$$Wear\ rate = \frac{\frac{material\ removed}{density}}{linear\ distance\ \times applied\ load} \quad (1)$$

The following data chart is obtained with the process just described:

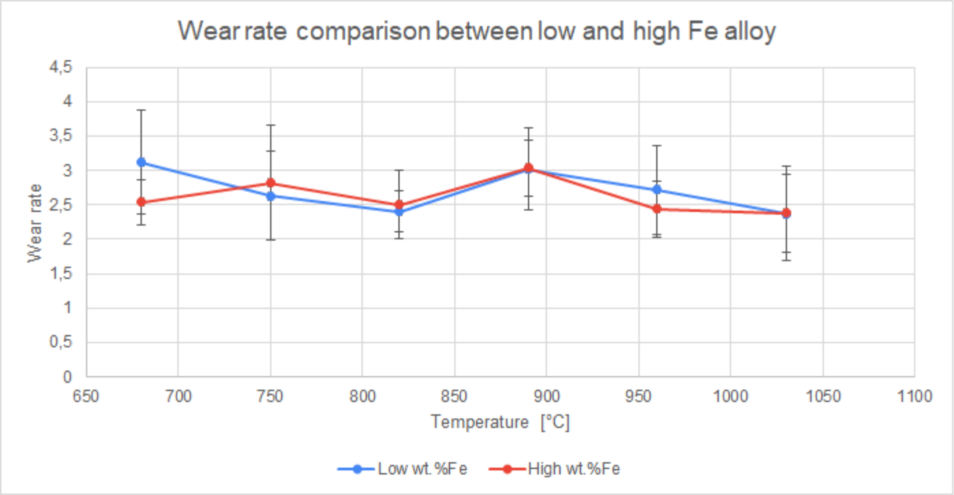

Fig 4.18*: Wear rate comparison for the alloys, as function of the casting temperatures*

From the chart it is noticeable that the wear rate of both alloys, taking into account their respective standard deviations too, remains about constant. That is contradictory to what the data suggests, especially for hardness. In fact, it would be reasonable to expect that the low-Fe alloy, that is harder than the high-Fe alloy, would also present a lower wear rate.

By comparing the data obtained for this alloy with an hypereutectic alloy, such as A390, it is evident that better wear resistance is present in the hypereutectic alloy, as shown in the following graph: [Fig. 4.19]

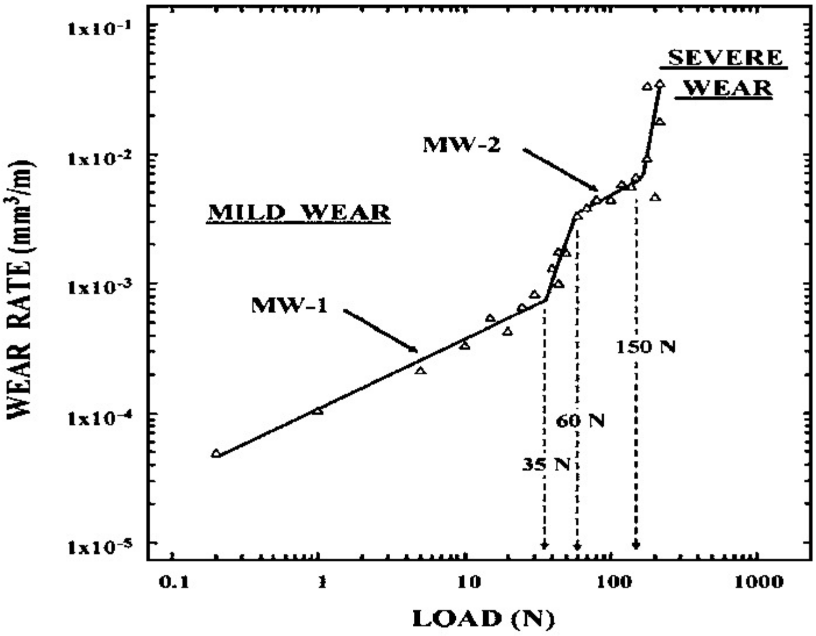

Fig. 4.19*: Wear rate of a hypereutectic alloy A390.*

In particular, in the graph above, the value of wear rate that must be considered is the one correspondent to a load of 1N.

Hence, what happens could be traceable to two factors: the balancing of the tribometer arm and porosity. Regarding the first aspect, the balancing of the tool holder arm is done manually by moving its center of gravity, displacing the two little weights on the side, so that the arm’s weight does not load on the sample. It is then the operator’s discretion to consider if the balancing has been done correctly, therefore it is possible that during the various tests, the load applied to the samples were greater than 1N, thus resulting in an increased loss of material and bigger wear rate. About the second factor, porosity, if the alumina sphere encounter cavities, their presence could affect the way that the sphere creeps on the surface and thus the results.

However in accordance to [23] the alloys’ wear resistance is mainly influenced by heat treatments, silicon content and intermetallic compound formation. Since these factors do not change significantly in this case study, the wear resistance results are about constant.

4.6 Hardness and wear rate comparison

As already marked, the low-Fe alloy results to have a higher hardness value compared to the high-Fe alloy. Considering that, according to the Archard equation (2), the hardness is strictly related to wear rate, it is logical to expect the wear rate of the low-Fe alloy to be lower than the high-Fe alloy one.

$$W = K\frac{F_n}{H} \quad (2)$$

Where:
W= Volume grind per unit of linear path [mm^3]; K= wear coefficient; Fn= normal load [N]; H= surface hardness [MPa]

Although, when the graphs are compared, it is evident that the alloys have a similar wear rate. It is possible that this behaviour is partly due to the higher amount of shrinkage porosities that form with a higher Fe wt.% [14].
Also, the way the experiment is conducted has a big impact on the amount of porosities formed in the alloy. Specifically, the fact that escape canals used by the gas to escape from the melt are missing, influences the process negatively, leading to a deterioration of the alloy performances by augmenting the amount of gas trapped inside the sample.

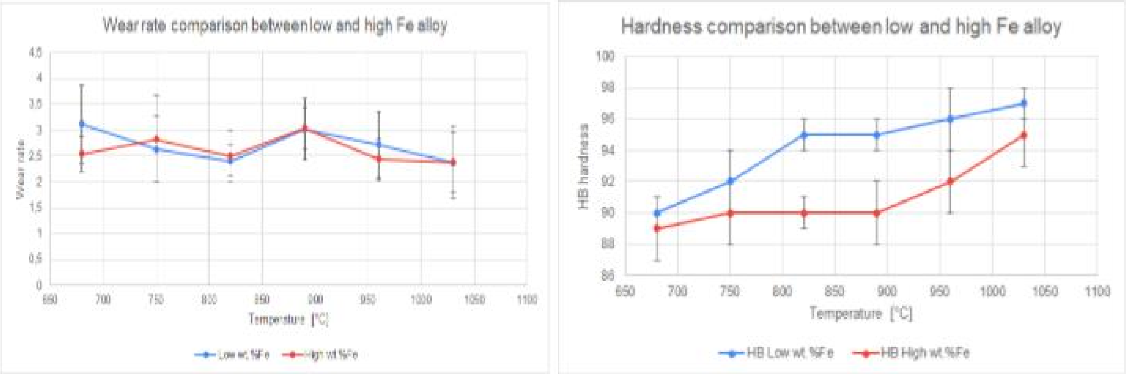

Fig. 4.20: *Hardness and wear rate comparison, as function of the casting temperatures*

In the following [Fig. 4.21] an example of the porosities formed in the samples are shown. The porosities are mainly detected in the High-Fe alloys with various dimensions. The biggest one depicted [Fig. 4.21] is the worst one produced out of all the samples. Even though at first the samples seem to be not presenting such inconvenience, when they are roughened for subsequent wear test the porosities start showing at different levels of depth in the sample.

Fig. 4.21: *Porosities formed in the High-Fe alloy*

4.7 Variance analysis

The procedure for the variance analysis is done by following the steps advised by [22]. The data related to the experiment are entered in minitab using the worksheet and appear thus organized:

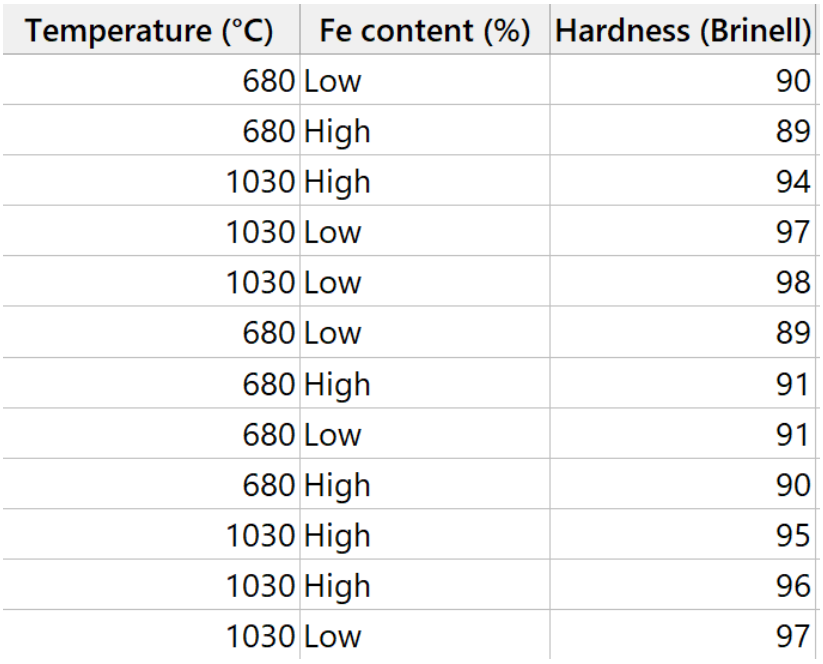

Temperature (°C)	Fe content (%)	Hardness (Brinell)
680	Low	90
680	High	89
1030	High	94
1030	Low	97
1030	Low	98
680	Low	89
680	High	91
680	Low	91
680	High	90
1030	High	95
1030	High	96
1030	Low	97

***Tab. 4.5**: Data used for the hardness minitab analysis*

By using the Balanced ANOVA function in Minitab, the following window will appear [Fig. 4.22]

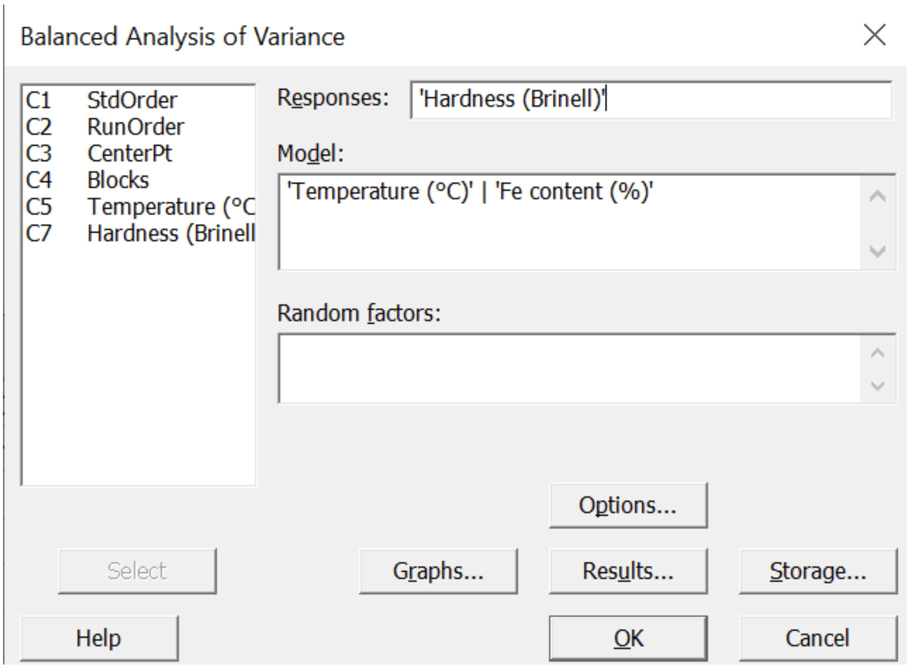
Balanced Analysis of Variance

C1 StdOrder
C2 RunOrder
C3 CenterPt
C4 Blocks
C5 Temperature (°C
C7 Hardness (Brinell

Responses: 'Hardness (Brinell)'

Model: 'Temperature (°C)' | 'Fe content (%)'

Random factors:

Fig. 4.22: Balanced Analysis of Variance window

By inserting *Hardness (Brinell)* in *Response* and the variables of interest in *Model*, minitab gives back the following output:

```
Analysis of Variance for Hardness (Brinell)

Source                          DF       SS       MS       F      P
Temperature (°C)                 1  114,083  114,083  136,90  0,000
Fe content (%)                   1    4,083    4,083    4,90  0,058
Temperature (°C)*Fe content (%)  1    4,083    4,083    4,90  0,058
Error                            8    6,667    0,833
Total                           11  128,917


S = 0,912871   R-Sq = 94,83%   R-Sq(adj) = 92,89%
```

Fig. 4.23: Output of the Balanced Analysis of Variance for Hardness

Since it is assumed =0,05 the critical value for F (obtained from the Fisher's F tables) is:

$$f_{0.05,1,8} = 5{,}32 \quad (3)$$

By analysing the F values in the minitab output it is noticeable that only the temperature F value satisfies:

$$F_{temperature} > f_{0.05,1,8} = 5{,}32 \quad (4)$$

Hence, temperature is the only factor that has a relevant effect on the response.

The same procedure is used to analyze the data of the wear test:

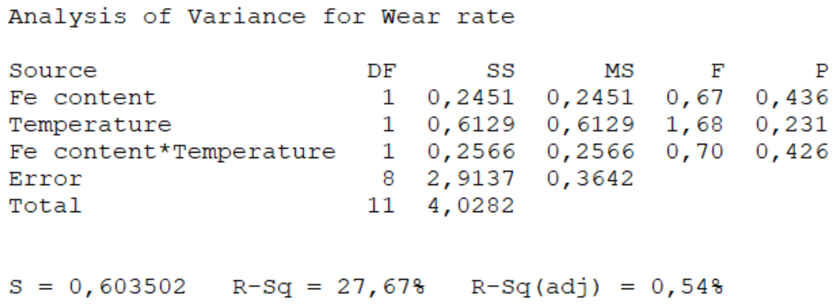

```
Analysis of Variance for Wear rate

Source                   DF      SS      MS     F      P
Fe content                1  0,2451  0,2451  0,67  0,436
Temperature               1  0,6129  0,6129  1,68  0,231
Fe content*Temperature    1  0,2566  0,2566  0,70  0,426
Error                     8  2,9137  0,3642
Total                    11  4,0282


S = 0,603502   R-Sq = 27,67%   R-Sq(adj) = 0,54%
```

Fig. 4.24: Output of the Balanced Analysis of Variance for Hardness

Hence, there are no factors that have a relevant effect on the response.

4.8 Empiric equations

Through this section is explained how experimental data were used to calculate two linear equations that given in input the Fe wt.% and the casting temperature, they return the Brinell hardness and wear rate respectively.

4.8.1 Procedure for the equation definition

To obtain the equation for hardness, the *Doe* function of Minitab is used, which is located in the section *Stat.* First, a matrix is created to describe the three values obtained for each test for each sample, with *Create factorial design.* Here, through *Design* it can be selected the number of replications, which represents the number of tests performed on each sample, in this case 3:

Number of replicates for corner points: 3.

By clicking on *Factors,* the factors that need to be considered in the analysis can be defined as follows, where *Temperature* represents the casting temperature and *Fe content* the Fe wt.%:

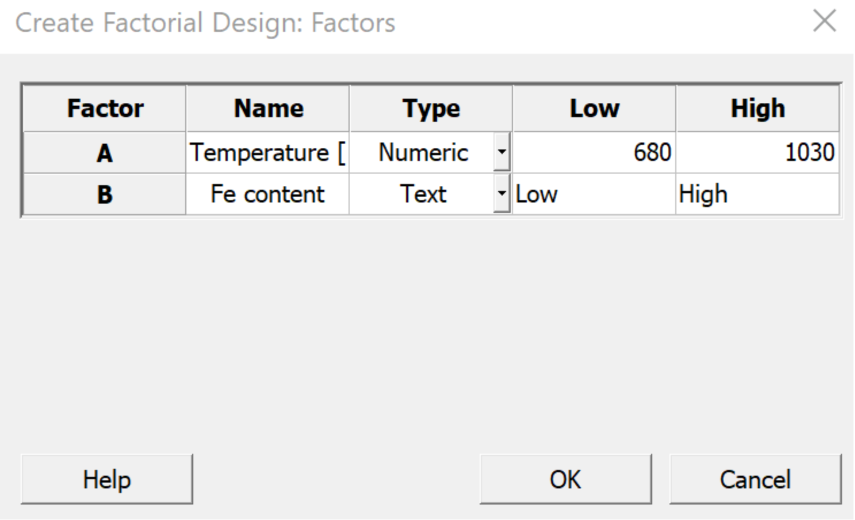

Create Factorial Design: Factors

Factor	Name	Type	Low	High
A	Temperature [	Numeric	680	1030
B	Fe content	Text	Low	High

Fig. 4.25: Compilation of factors in Create Factorial design

Once the *OK* button is clicked, the following matrix is given:

Tab. 4.6*: the matrix obtained from Create Factorial Design*

Temperature (°C)	Fe content (%)
680	Low
680	High
1030	High
1030	Low
1030	Low
680	Low
680	High
680	Low
680	High
1030	High
1030	High
1030	Low

Now, the third column is added to indicate the results of the hardness tests:

Tab. 4.7*: the matrix with the Hardness values*

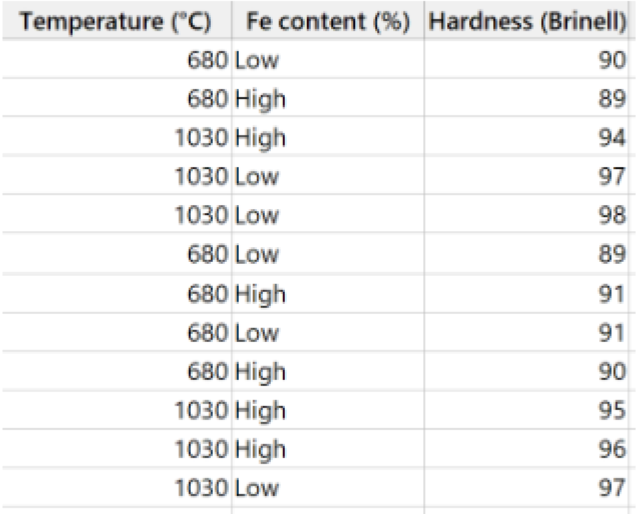

Temperature (°C)	Fe content (%)	Hardness (Brinell)
680	Low	90
680	High	89
1030	High	94
1030	Low	97
1030	Low	98
680	Low	89
680	High	91
680	Low	91
680	High	90
1030	High	95
1030	High	96
1030	Low	97

Once the matrix is obtained, the process continues by clicking on *Doe*, function *Analyze factorial design*, where the Hardness (Brinell) has to be added as *Responses*. On *Terms,* the following setting has to be specified: *Include terms in the model up to: 2*, to include terms up to the second order (so *Temperature (°C), Fe content (%)* and the interaction between them).

On *Graphs* the option *Pareto* has to be flagged*,* which will be subsequently used; then is set at 0,05, where corresponds to the confidence level.

The results of these operations are: the equation written at the beginning of Chapter 4.8 and the Pareto graph [Fig.4.26] from which it can be noticed that the *Fe content (%)* and the interaction between *Fe content (%)* and *Temperature (°C)* are under the confidence level and, for these reason, they are not considered for the equation. Therefore, the same procedure is repeated by starting at *Analyze factorial design,* where now on *Terms* the option *Include terms in the model up to:* is set to 1 so that only temperature is considered. From this point on, the procedure described above needs to be repeated; the final equation (5) is obtained.

The same procedure is used to analyze the data of the wear test, with the difference that all the Factors (*Temperature (°C)*, *Fe content (%)* and the interaction between them) are found to be under the confidence level, as shown in [Fig.4.28]. Therefore, it is not possible to deduct an equation for the wear rate as a function of Fe content and casting temperature.

4.8.2 Equation description

After inserting the hardness values, minitab gives back the following equation:

$$Hardness\ [HB] = 78{,}02 + 0.01762\ Temperature + 2{,}27\ Iron\ content -$$
$$-0{,}00333\ Temperature \times Iron\ content$$

In [Fig. 4.26] the resulting Pareto graph is shown.

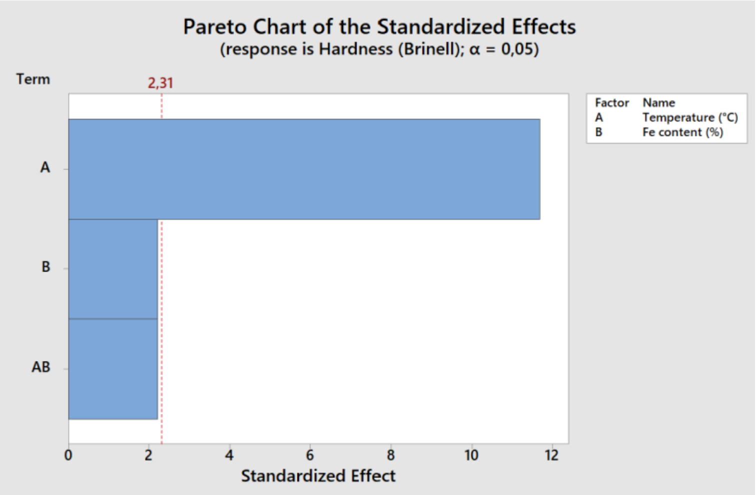

Fig. 4.26: Pareto Chart for Hardness

From the Pareto graph, obtained using as Response the data related to hardness for the two alloys at casting temperature of 680°C and 1030°C respectively, it's clear that it isn't significantly influenced by the iron content and the interaction between Fe wt.% and the casting temperature.

Therefore, considering that hardness varies only in function of casting temperature, the following equation could be achieved:

$$Hardness\ [HB] = 78{,}02 + 0.01762\ Temperature\ (5)$$

Comparing the output values given back from the equation with the experimental values, the following graph is obtained:

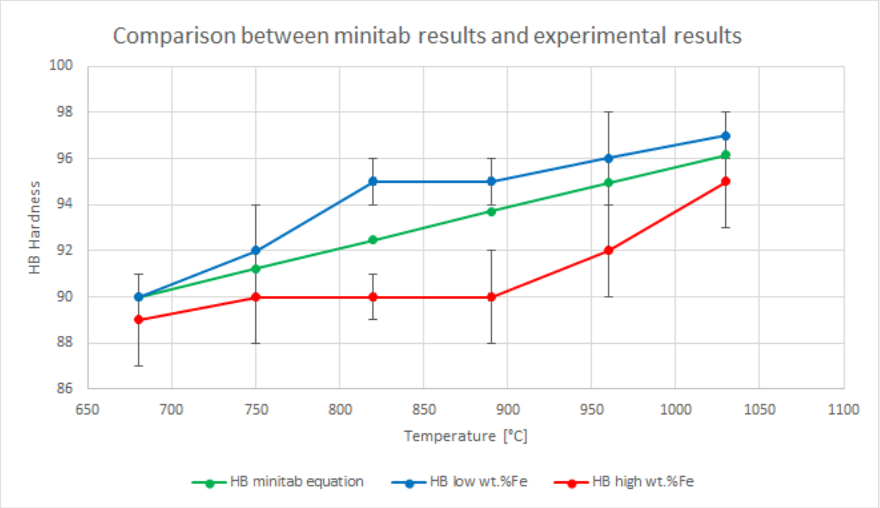

Fig. 4.27: Comparison between minitab results and experimental results as function of the casting temperatures

Regarding the wear rate, from the Pareto graph is noticeable that neither temperature nor Fe wt.% seems to influence it:

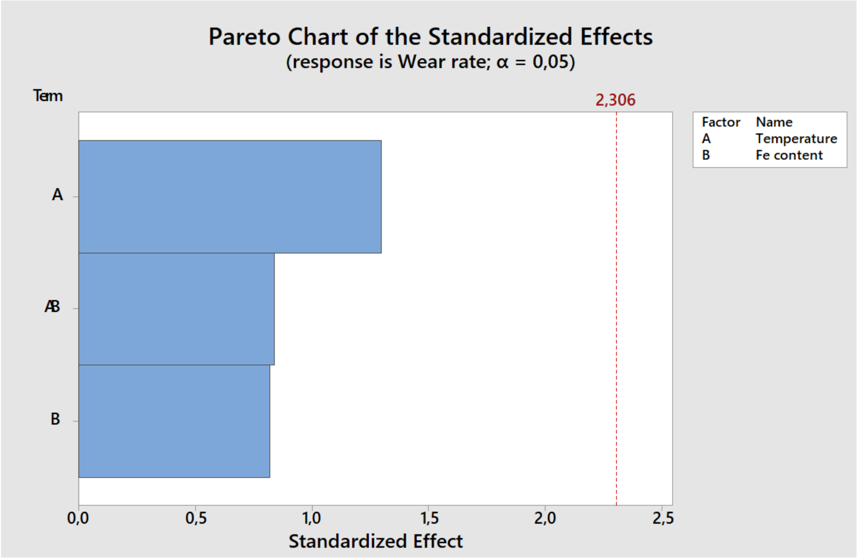

Fig. 4.28: *Pareto chart for wear rate*

Conclusions

The target of this thesis is to study the effect of Fe content on microstructural and mechanical wear properties in innovative aluminium alloys for pistons application in the automotive sector, particularly how the mechanical properties vary as the Fe content and the casting temperature change.

Regarding the morphological analysis, it is observed that the amount of β-phase decrements progressively as the casting temperature increases. In particular, the lower the Fe wt.%, the lower the temperature at which β disappears is. Specifically, from 820°C up, for the low-Fe alloy, and from 890°C up for the high-Fe alloy, the β-phase amount is close to null.

As expected, the Fe-rich compounds grain refines as the casting temperature rises.

Moreover, by rising the bath temperature, the morphology of the α-phase is changed; in fact, for casting temperatures lower than 820°C it mainly presents a polyhedral morphology, while as for temperatures higher than 820°C the Chinese-script like morphology tends to take over. Nevertheless, it has been derived from literature that the compounds' morphology does not influence the material hardness.

On the other hand, hardness results to be correlated to bath temperature since higher temperatures lead to a better grain refinement, which brings better performances for the alloy.

Concerning the wear resistance, such property should be correlated to the material hardness; although, our data do not show this relation. This is due to a higher presence of porosities in materials obtained with high casting temperatures and with higher Fe wt.%, which are supposed to be the hardest ones.

According to literature, as the iron content increases, shrinkage porosities increase too. In fact, the high-Fe alloy sample suffered severe porosities that inevitably influenced the various measurements. Hence, with a higher iron content it is necessary to pay particular attention during the casting process.

Therefore, it results to be more effective to use alloys with lower Fe wt.% in order to avoid casting and porosity linked adversities, while still obtaining significant improvements for the alloy performances thanks to the iron content.

Finally, in the present case the low-Fe alloy processed with the casting temperature of 820°C results to be the best economic compromise for hardness and wear resistance, along with good grain refinement.

Bibliography

[1] Fig 1.1 Marlen Bertram, Kenneth J. Martchek, Georg Rombach “Material Flow Analysis in the Aluminum Industry” Journal of industrial ecology, 1st December 2009, pp. 652

[2] Fig. 1.2: Bachelor thesis presentation PPT

[3] Fig. 1.3: Bachelor thesis presentation PPT

[4] Fig. 1.4: Rahman M, Rosli B. “Assessment of Fatigue Life Behaviour of Cylinder Block for Free Piston Engine Using Frequency Response Approach”, Research Journal of Applied Science 3 (1): 2008.

[5] Fig. 1.5: https://www.ms-motorservice.com/it/technipedia/post/danni-ai-pistoni-e-relative-cause/

[6] Tab. 1.1: https://it.qaz.wiki/wiki/Prices_of_chemical_elements

[7] Stefano Ferraro, Alberto Fabrizi, Giulio Timelli ”Evolution of sludge particles in secondary die-cast aluminum alloys as function of Fe, Mn and Cr contents”, Materials Chemistry and Physics 153 (2015), pp. 168-179.

[8] G.Timelli, E.Fiorese, ”Metodi di neutralizzazione del Fe in leghe Al-Si da fonderia”, La Metallurgia Italiana - n. 3/2011, pp. 9-23.

[9] Cameron M. Dinnis, John A. Taylor, Arne K. Dahle, ”As-cast morphology of iron-intermetallics in Al–Si foundry alloys”, Scripta Materialia 53 (2005), pp.955–958

[10] Alberto Fabrizi, Giulio Timelli, Stefano Ferraro, Franco Bonollo, ”Evolution of Fe-rich compounds in a secondary Al–Si–Cu alloy: influence of cooling rate”, International Journal of Materials Research, July 21, 2015, pp. 719-724.

[11] C.M. Dinnis, J.A. Dinnis, J.A. Taylor, and A.K. Dahle “Interactions between Iron, Manganese, and the Al-Si Eutectic in Hypoeutectic Al-Si Alloys”, Metallurgical and material transactions A, Vol. 37A, november 2006, pp. 3283-3291.

[12] Fig. 1.6:”, Alberto Fabrizi, Giulio Timelli, Stefano Ferraro, Franco Bonollo, ”Evolution of Fe-rich compounds in a secondary Al–Si–Cu alloy: influence of cooling rate”, International Journal of Materials Research, July 21, 2015, pp. 719-724.

[13] Fig. 1.7: Cameron M. Dinnis, John A. Taylor, Arne K. Dahle, ”As-cast morphology of iron-intermetallics in Al–Si foundry alloys”, Scripta Materialia 53 (2005), pp.955–958

[14] Z. Ma, A.M. Samuel, F.H. Samuel, H.W. Doty, S. Valtierra ”A study of tensile properties in Al–Si–Cu and Al–Si–Mg alloys: Effect of -iron intermetallics and porosity”, Materials Science and Engineering A 490 (2008), pp. 36–51

[15] Giulio Timelli, Alberto Fabrizi, Simone Vezzù, Alessandro De Mori, “Design of Wear-Resistant Diecast AlSi9Cu3(Fe) Alloys for High-Temperature Components”, Metals 2020, 10, 55, pp. 1-16.

[16] Karthikeyan Rangaraju and Neelakrishnan Subramanyan “Influence of Intermetallic Compounds on Age Hardening of Gasoline Pistons in Engine Operations”, Journal of Materials Engineering and Performance, Vol. 30(1), January 2021, pp. 177-189.

[17] Dehong Lu, Yehua Jiang, Guisheng Guan, Rongfeng Zhou, Zhenhua Li, Rong Zhou “Refinement of primary Si in hypereutectic Al–Si alloy by electromagnetic stirring”, Journal of Materials Processing Technology, Volume 189, Issues 1–3, 6 July 2007, pp. 13-18.

[18] Marco V. Boniardi, Andrea Casaroli, “L’alluminio e le sue leghe”, Versione 4 (19-02-2013).

[19] https://www.raffmetal.it/scarica_file.asp?c=/dati/SearchAlloy/ITA/&f=EN46100.pdf

[20] Fig. 4.16 https://img.directindustry.it/images_di/photo-mg/16352-15522996.jpg

[21] Fig. 4.17 https://www.astorispa.it/catalogo/prodotto/comparatore-mitutoyo-575-121-19920/U122619%20?utm_campaign=Kelkoo%26utm_medium=item_list%26cmpcode=7&from=kelkooit

[22] Guido Berti, Manuel Monti, Luigi Salmaso “Introduzione alla metodologia DOE nella sperimentazione meccanica - Disegno sperimentale e superfici di risposta” pp.178-193

[23] “ASM handbook: Friction, lubrication and Wear Technology”, Vol. 18